



Coordinatively unsaturated atomically dispersed $\text{Pt}^{+2}\text{-N}_4$ sites on hexagonal nanosheet structure of $\text{g-C}_3\text{N}_4$ for high-performance photocatalytic H_2 production

Tahereh Mahvelati-Shamsabadi^a, Kailash Chandra Bhamu^a, Seong-hun Lee^{b,c},
Thanh Truong Dang^a, Vu Hoang Khoi^a, Seung Hyun Hur^a, Won Mook Choi^a, Sung Gu Kang^{a,*},
Tae Joo Shin^{b,c,**}, Jin Suk Chung^{a,*}

^a School of Chemical Engineering, University of Ulsan, Ulsan 44610, Republic of Korea

^b Unist Central facilities, Ulsan National Institute of Science and Technology (UNIST), 50 Unist-gil, Ulsan 44919, Republic of Korea

^c Graduate School of Semiconductor Materials and Devices Engineering, Ulsan National Institute of Science and Technology (UNIST), 50 Unist-gil, Ulsan 44919, Republic of Korea

ARTICLE INFO

Keywords:

Single atom catalysis
Electronic metal-support interactions
Local coordination environment
Photocatalytic hydrogen production

ABSTRACT

Developing active and stable metal single-atom catalysts is technically challenging. The electronic interactions between the metal site and its supports play a key role in altering electronic properties for the creation of more reactive and stable centers. The local environment of a single-atom catalyst directly affects its stability and reactivity. Herein, we describe the formation of coordinatively unsaturated atomically dispersed Pt^{+2} sites ($\text{Pt}^{+2}\text{-N}_4$) on hexagonal nanosheets of $\text{g-C}_3\text{N}_4$ ($\text{Pt}_1\text{-HCN}$). This structure with Pt loading of 0.38 wt% exhibited a superb photocatalytic hydrogen evolution rate of $2900 \mu\text{mol g}^{-1} \text{h}^{-1}$ which was 5.6 times higher than that of the reactive Pt_1 sites ($\text{Pt}^{+4}\text{-N}_5$) on bulk ($\text{Pt}_1\text{-BCN}$). The comprehensive advance spectroscopic analysis combined with DFT calculations revealed that the strong electronic metal-support interactions between Pt_1 and HCN effectively reduced the adsorbed Pt^{+4} sites into Pt^{+2} and create favorable uniform $\text{Pt}^{+2}\text{-N}_4$ moieties at low Pt loading for water adsorption, dissociation, and H_2 evolution.

1. Introduction

Hydrogen fuel has attracted considerable attention due to its extremely high weight energy density (122 kJ g^{-1}) and pivotal role in solving the energy crisis and environmental problems [1–3]. Hydrogen is a truly zero-emission and zero-pollution fuel source because water will be the final product of hydrogen fuel combustion, regardless of how it is used [4]. Currently, the majority of required H_2 is produced from methane steam reforming [5]. Photocatalytic water splitting is one of the most promising techniques for producing sustainable H_2 [6]. However, its sluggish oxidation reaction kinetics require sacrificial agents in the system to improve hydrogen production efficiency. Despite great efforts to create and introduce highly efficient photocatalytic H_2 -evolution systems, photocatalysts still exhibit low efficiency due to non-effective charge-carrier generation and recombination [7]. Loading photocatalysts with a co-catalyst is an effective method to suppress

charge carrier recombination [8–11]. They simultaneously trap electrons and provide active reduction sites for water molecules [9]. Noble metals, especially Pt and Pt-based alloys, are considered the best co-catalysts for photocatalytic hydrogen evolution (PHE) reactions [12–14]. However, the cost and low abundance of Pt severely limit its application.

The development of advanced characterization techniques revealed that coordinatively unsaturated metal atoms at the surface of nanoparticles (NPs) are usually active sites for catalysis [15]. The catalytic performance of metal nanoparticles can be tuned by adjusting the size, morphology, and distribution of atoms at the catalyst surface [16]. Recently, supported atomically dispersed metal catalysts with maximized atom efficiency, exclusive site homogeneity, and spatial site confinement have drawn considerable attention in a variety of catalysis fields [1,17–22]. By reducing the particle size to atomically dispersed atoms with ionic character, metal-support interactions can become

* Corresponding authors.

** Corresponding author at: Unist Central facilities, Ulsan National Institute of Science and Technology (UNIST), 50 Unist-gil, Ulsan 44919, Republic of Korea.

E-mail addresses: sgkang@ulsan.ac.kr (S.G. Kang), tjshin@unist.ac.kr (T.J. Shin), jschung@ulsan.ac.kr (J.S. Chung).

exceptionally important due to the significant enhancement of surface-free energy and substantial charge transfer [23–27]. Due to electronic interactions, the support can induce considerable electronic perturbations to atomic metals by modifying metal d-band orbitals [28–30]. This restructures electronic metal-support interactions in terms of charge transfer, which leads to significant catalytic activity due to the manipulation of reactants' adsorption and dissociation [15,31,32]. Introducing single Pt atoms as the co-catalyst for PHE can be an effective strategy to dramatically reduce the usage of Pt metals and also create well-defined active sites. However, direct bonding between Pt ions and coordination sites in the support structure modulates charge separation and transfer, leading to improved activity. Still, single-atom photocatalysts for PHE are early in development [33].

The interest in the reactivity of supported single Pt atoms (Pt_1) for PHE mostly comes from the maximized metal utilization efficiency. However, good knowledge of the metal-support interaction (MSI), mass loading, uniformity of active sites, and coordination configuration is the most crucial parameter for deeply understanding their distinct reactivity [34–36]. Coordinatively unsaturated single atomic centers are favorable for adsorbate molecules to interact and reactively participate in the catalytic cycle. Hence, modulating the coordination configuration and the oxidation state of single atomic sites is believed to be essential for the optimization of the catalytic properties of single atoms. Consequently, simply synthesizing single-atom alternatives of traditional Pt nanoparticles as co-catalysts is not an ideal tactic, the experimental and theoretical investigations are mandatory to define the metal-support arrangements representing the best performance [37,38].

Graphitic carbon nitride ($g-C_3N_4$) is a well-known photocatalyst that can be perfectly designed for strong visible light utilization and charge separation efficiency. Moreover, it also provides isolated confined anchoring sites for the coordination of Pt ions as the co-catalyst and reactive sites for PHE as it contains an ordered periodic motif of triangular nitrogen cavities with six unsaturated pyridinic nitrogen atoms [24,39–45].

In this work, we studied photocatalytic hydrogen evolution reaction for isolated atomic Pt moieties on either bulk $g-C_3N_4$ or hexagonal nanosheets of $g-C_3N_4$ as the light-sensitive supports. Graphitic carbon nitride supports provided the essential photovoltage to drive the hydrogen evolution reaction on the isolated Pt sites in the structure. The Pt_1-N_x moieties were produced on $g-C_3N_4$ through a simple wet-impregnation method using the commonly available Pt precursor of $H_2PtCl_6 \cdot 6H_2O$. The Pt_1 sites on hexagonal $g-C_3N_4$ exhibited the highest reactivity toward the PHE in the basic medium with a hydrogen evolution rate of $763 \mu\text{mol mg}_{Pt}^{-1} \text{h}^{-1}$ compared to the $136 \mu\text{mol mg}_{Pt}^{-1} \text{h}^{-1}$ for the Pt_1 sites on the bulk $g-C_3N_4$. Moreover, the Pt NPs counterparts on hexagonal nanosheets showed a dramatically decreased activity about 18 times lower than that of Pt_1 sites. The XANES results of the impregnated samples before the annealing process demonstrated that nitrogen pores dynamically participated in ligand exchange and Pt coordination. Consequently, the Pt-N coordination peak sharply appeared in the EXAFS spectra of impregnated samples without any observable peak of Pt-Cl scattering from the H_2PtCl_6 precursor. Comprehensive spectroscopic characterization, DFT calculations, and electrochemical analyses were applied to study the origin of highly-active Pt_1 sites on HCN toward HER as well as their deactivation mechanism after high-temperature annealing. The detailed analysis revealed that HCN actively reduces adsorbed Pt^{+4} sites to Pt^{+2} at a low Pt concentration of $< 1 \text{ wt}\%$ due to a higher zeta potential value and strong electronic metal-support interactions and creates mostly stable ($Pt^{+2}-N_4$) active sites. DFT calculations revealed that Pt^{+2} ions accelerated water molecule dissociation compared to Pt^{+4} by reducing the kinetic energy barrier and facilitating hydrogen evolution through reducing H adsorption energy. Also, their favorable coordinated environment provides multiple water molecule adsorption due to their unsaturated nature of Pt centers compared to less saturated $Pt^{+4}-N_5$ moieties and unreactive fully saturated $Pt^{+4}-N_6$ on BCN. Moreover, thermal treatment of Pt_1 -HCN at

elevated temperatures reduced the four nitrogen-coordinated Pt centers as well as the Pt oxidation state.

2. Experimental

2.1. Synthesis of cyanuric acid-melamine complex (CM complex)

Cyanuric acid and melamine with the same molar ratio of 0.19 M were dispersed in de-ionized water in two separate beakers in an ultrasonic bath operating at an amplitude of 20 KHz for 10 min. After that, both dispersions were mixed in a larger beaker, and the mixture was ultrasonicated for another 15 min at 50°C . During the ultrasonication process, the mixture was frequently checked to disperse any possible large aggregates. The obtained homogenous diluted mixture was dried in a conventional electrical oven at 80°C for 48 h. The final white CM complex precursor had a very light and layered structure. (Fig. S2 and S3, show the FESEM images and XRD patterns of the as-prepared CM complex).

2.2. Synthesis of hexagonal $g-C_3N_4$

The $g-C_3N_4$ (HCN) with a hexagonal rosette structure was synthesized by heating the CM complex at 500°C for 3 h with a ramping rate of 5°C min^{-1} in an open alumina crucible placed inside the tubular furnace under an Ar atmosphere (500 mL min^{-1}).

2.3. Synthesis of bulk $g-C_3N_4$

The bulk $g-C_3N_4$ (BCN) was synthesized by heating dicyandiamide at 540°C for 4 h with a heating rate of 5°C min^{-1} in a closed alumina crucible placed inside a conventional muffle furnace.

2.4. Synthesis of Pt_x -HCN, and Pt_x -BCN photocatalysts

All Pt_x -HCN (x refers to the form of Pt in the $g-C_3N_4$ structure, Pt_1 indicates the presence of single atomic Pt sites, Pt_{mix} is the mixture of single atomic, clusters, and nanoparticles of Pt) were prepared by a conventional wet impregnation method. Before loading the Pt precursor ($H_2PtCl_6 \cdot 6H_2O$), the $g-C_3N_4$ supports were ultrasonicated for 1 h in an ultrasonic bath with a frequency of 20 kHz. After loading support materials (BCN, and HCN) with the desired level of Pt in 6 h at 70°C in an appropriate synthesis volume, the impregnated supports were washed at least three times with deionized water to remove excess amounts of unadsorbed Pt precursor followed by drying at 80°C for 12 h. The annealing process (thermal activation process) was conducted at two different temperatures of 125 and 325°C for 1 h with a heating rate of $3.3^\circ\text{C min}^{-1}$ in an Ar atmosphere (500 mL min^{-1}) inside a tubular furnace.

2.5. Synthesis of Pt_{NPs} -HCN

First, 50 mg of HCN support was dispersed in DI water for 1 h under ultrasonication. After that, a certain amount of an aqueous solution of $H_2PtCl_6 \cdot 6H_2O$ (3 wt% of Pt) was added to the dispersion and mixed for 15 min. Then, the dispersion was irradiated by the Xenon lamp with a power density of 300 W equipped with an AM 1.5 G filter for 6 h. During the photo deposition, the reactor was purged with Ar gas. After loading, the sample was carefully washed and dried in the vacuum oven at 100°C for 24 h. Pt_{NPs} indicate the presence of Pt nanoparticles.

2.6. Photocatalytic hydrogen measurement

Photocatalytic hydrogen production was measured in a gas-closed system with a quartz cell reactor using 1 mg for Pt_1 -HCN samples, 20 mg for Pt_{NPs} -HCN, and 10 mg for Pt_1 -BCN samples. Powder samples were well dispersed using 15 min ultrasonication in 50 mL of a 20 V%

aqueous solution of triethanolamine as a hole scavenger (the catalyst dosage and the reaction volume were optimized by checking the activities at different catalyst concentrations). After evacuation with Ar gas for 30 min, the cell reactor containing the sample was irradiated from above by a 300 W Xe lamp (Asahi Spectra) equipped with an AM 1.5 G filter. The light intensity was measured and fixed at 100 mW cm^{-2} by controlling the distance between the reactor and the lamp (at 15 cm). The reaction temperature was kept at 10°C using a water jacket. The evolved H_2 gas was measured via an automatic injection, online gas chromatograph (Agilent 8890 G-G3540A) with a thermal conductive detector (TCD) and a Carboxen 1000 column (Sigma-Aldrich).

2.6.1. Calculation of mass activity and turnover frequency (TOF)

The mass activity and TOF activity of the catalysts were calculated according to the following equations:

$$\text{Mass activity} = \frac{nH_2}{\text{mg Pt} \cdot \tau} \quad (1)$$

$$\text{TOF for Pt deposited photocatalyst} = \frac{n H_2}{n \text{ Pt} \cdot \tau} \quad (2)$$

2.7. Electrochemical measurements

Electrochemical impedance spectroscopy measurements were carried out in a typical three-electrode system with an electrochemical workstation at room temperature and using a graphite rod as the counter electrode and saturated Hg/HgO as the reference electrode. To prepare the working electrode, 2 mg of catalyst and 10 μL of Nafion solution (5 wt%) were ultrasonically dispersed in a 1 mL water/isopropanol

solution (vol, 3:1) for 20 min to form a homogenous ink. Then, 1 mL of the ink was drop-casted on the surface of a glassy carbon electrode four times. Subsequently, the coated electrode was dried under an IR lamp for 1 h before use. The measurements were done by first applying a 0.6 V (vs Hg/HgO) potential for at least 10 min. Then, the measurement was conducted in a frequency range from 100 mHz to 100 kHz.

The computational calculation details are brought in the [supplementary information](#).

3. Results and discussion

3.1. Synthesis and structural characterization

The overall synthetic procedure to prepare isolated Pt species on hexagonal and bulk g- C_3N_4 , $\text{Pt}_1\text{-HCN}$, and $\text{Pt}_1\text{-BCN}$, respectively, is illustrated in Fig. 1a. The interactions between H_2PtCl_6 and g- C_3N_4 supports seem to be electrostatic interactions of $[\text{PtCl}_x]^{6+}$ species and dispersed $[\text{HCN}]^{\delta-}$ and $[\text{BCN}]^{\delta-}$. The measured zeta potentials on HCN and BCN surfaces were around -38.3 and -20.4 mV, respectively. As they have opposite interfacial charges to $[\text{PtCl}_x]^{6+}$ species, the positive Pt species were spontaneously adsorbed on g- C_3N_4 supports during the wet-impregnation step. This method can attenuate the accumulation of the adsorbed $\text{H}_2\text{PtCl}_6 \cdot 6\text{H}_2\text{O}$ during the impregnation and thermal activation step due to the strong coordination ability of nitrogen atoms in the g- C_3N_4 structure. We expect stronger electronic interactions between HCN and $[\text{PtCl}_x]^{6+}$ in comparison with BCN because HCN has a higher negative surface charge. The well-built electronic interactions can further lead to a higher reactivity and stability of Pt single atomic sites. After the impregnation process, the impregnated HCN and BCN supports were thoroughly washed three times with DI water and dried in

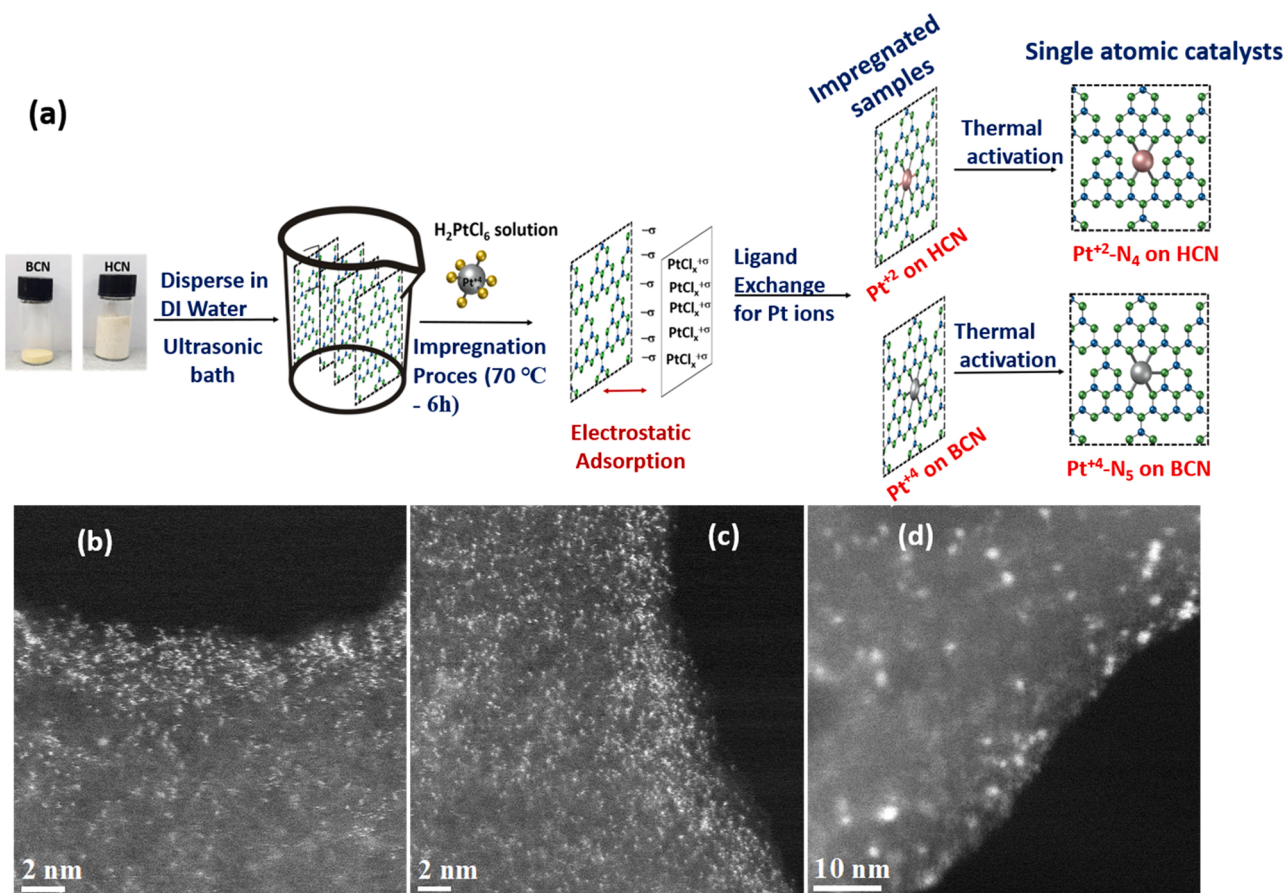


Fig. 1. (a) Scheme of synthesis procedure of $\text{Pt}_1\text{-HCN}$, and High-resolution HAADF-STEM images of Pt-HCN samples, (b) $\text{Pt}_1\text{-HCN}$ (0.38%)–125, (c) $\text{Pt}_1\text{-HCN}$ (0.75%)–125, and (d) $\text{Pt}_{\text{mix}}\text{-HCN}$ (0.75%)–125.

a conventional oven overnight. Then, the dried impregnated HCN and BCN were thermally activated at 125 °C and 325 °C in a tubular furnace in an argon atmosphere.

To evaluate the effect of different Pt loadings on the Pt active site structures and reactivity, we extended the synthetic approach to prepare a broad range of Pt_x-HCNs with various Pt loadings of 0.38, 0.75, 1.5, and 3.5 wt%. Pt₁-BCN samples were also prepared at 0.38 and 0.75 wt% to study the effect of the support structure on the electronic and local geometry of Pt₁ sites and their reactivity.

Field emission scanning electron microscopy (FESEM) images (Figs. S4 and S5) showed the formation of small separated hexagonal rosette nanosheets for the HCN sample that can be compared with the stacked layered structure of BCN [46,47]. The atomic structure of Pt sites on HCN was imaged by high-angle annular dark-field scanning transmission electron microscopy (HAADF-STEM). The HAADF-STEM images proved that Pt species are atomically dispersed on HCN support at low Pt loadings (<1 wt%), Fig. 1b and c, but a mixture of Pt

isolated atoms, clusters, and nanoparticles are formed when the loading exceeded 1 wt% (Fig. 1d and Fig. S7). Fig. 1b and c and Fig. S6 indicate uniformly distributed isolated Pt atoms over the entire HCN matrix at 0.38 and 0.75 wt%. The Pt loading amounts were measured by inductively coupled plasma mass spectroscopy (ICP-MS), Table S1.

Additionally, Fig. S8 shows Pt nanoparticles with an average size of about 1.5 nm on HCN, which were obtained via photo-deposition of H₂PtCl₆•6 H₂O over 6 h. The Pt loading value was 3.1 wt%.

The X-ray diffraction patterns of Pt-HCN and Pt-BCN samples with different Pt values were almost the same as pristine HCN and BCN, Fig. S9. They did not show any Pt-containing crystal phase, which is due to the insensitivity of X-ray diffraction to small nanoparticles. Except for Pt_{NPs}-HCN, the XRD pattern shows the existence of a PtO phase (Fig. S9a). All samples exhibited two typical main peaks of g-C₃N₄, including (100) at about 13.12° and (002) at about 27.5°. The broader and lower intensity peaks in HCN in comparison with the BCN demonstrate the almost amorphous nature of g-C₃N₄ in HCN (Fig. S9a and b)

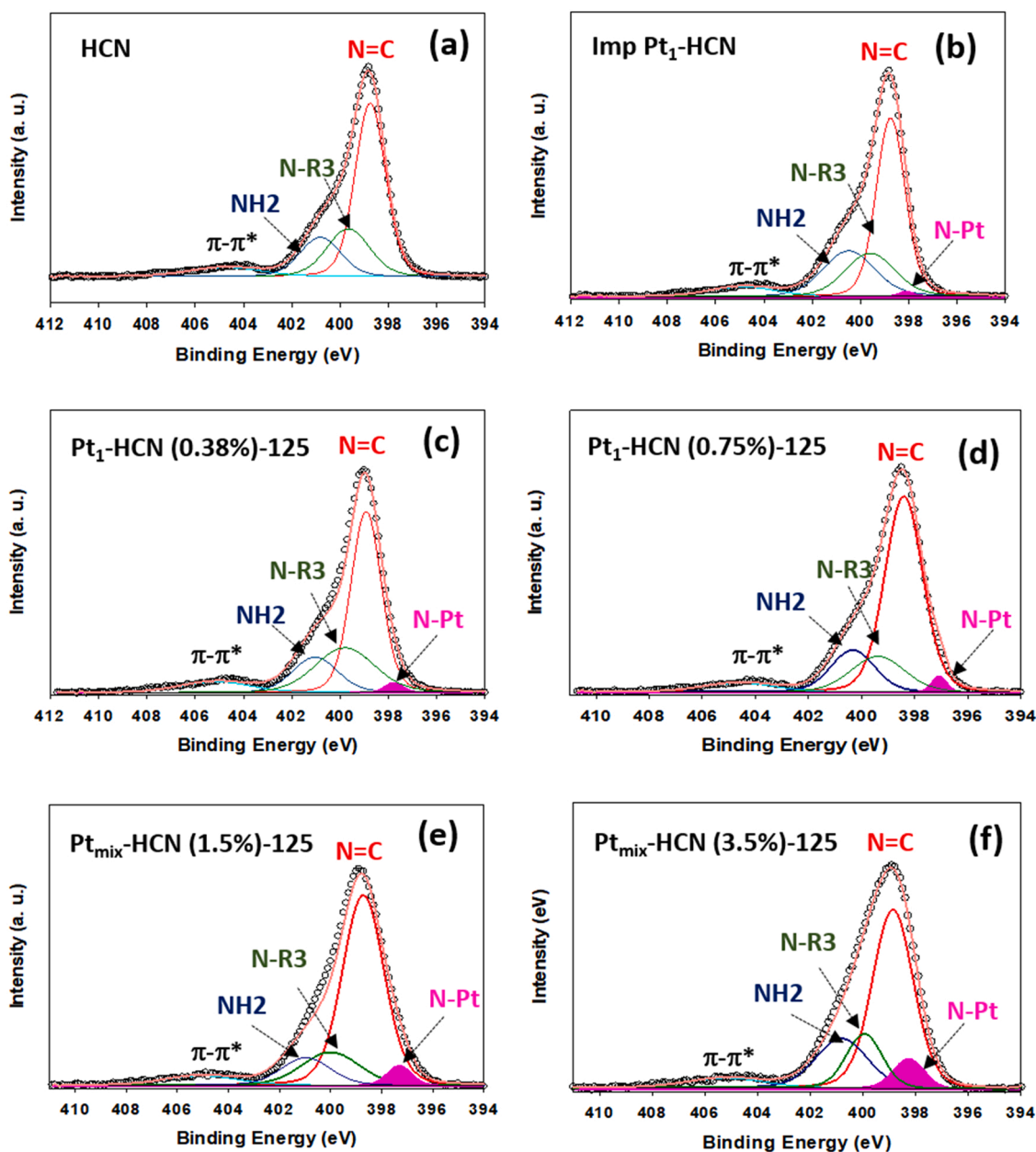


Fig. 2. Deconvoluted N1s XPS spectra of (a) HCN, (b) Imp Pt-HCN, (c) Pt₁-HCN (0.38%)–125, (d) Pt₁-HCN (0.75%)–125, (e) Pt_{mix}-HCN (1.5%)–125, and (f) Pt_{mix}-HCN (3.5%)–125.

[48]. Hence, the XRD results confirmed the successful construction of g-C₃N₄ with a graphitic nature for both HCN and BCN.

The configuration of g-C₃N₄ and Pt-loaded g-C₃N₄ was further confirmed by XPS investigation. The N1s spectra of HCN and BCN demonstrated the existence of three types of nitrogen including N₂C (two coordinated nitrogen, N_{sp2}), N₃C (three coordinated nitrogen, N_{sp3}), and NH₂ in structures with binding energies of 398.5, 399.8, and 400.6 eV, respectively (Fig. 2a and Fig. S10b) [43,46]. Interestingly, a new peak appears at a lower binding energy area of N₂C for the Pt-deposited samples in both HCN and BCN structures. This can be assigned to the chemical bonds of N-Pt (Fig. 2b-f). The graphs related to BCN samples are included in the supplementary information, Fig. S10 [39]. The surface area relative fraction of the N-Pt feature (Table S2, and S3) increased with increasing Pt loading, which suggests the conversion of the free nitrogen pore sites in the g-C₃N₄ framework into Pt-N_x moieties. These results exhibited mutual interactions between the Pt species and the g-C₃N₄ matrix in the six folded nitrogen cavities as well as the electron transfer between them. Moreover, the high-resolution C1s spectra of all pristine and Pt deposited supports (Fig. S10a and c, and S11) indicate the typical components of carbon at 284.8 and 287.6 eV,

which can be indexed as C=N and C-C/C=C bonds, respectively. An extra peak around 286.2 eV was assigned to the carbon in the form of cyano groups due to the presence of defect sites in the basal plane [49].

Pt 4f X-ray photoelectron spectroscopy was applied to verify the presence of Pt species and determine their electronic states. The deconvoluted Pt 4f XPS spectrum of almost all prepared Pt_x-HCN catalysts exhibited two doublets of Pt 4f_{7/2} and Pt 4f_{5/2}, which were very close to Pt⁺² (in PtO at 72.7 eV and Pt(OH)₂ at 74.0 eV) and Pt⁺⁴ (in PtO₂ at 74.9 eV) species. The Imp Pt₁-HCN with a Pt loading of 0.75 wt % demonstrated a sharp doublet (peaks at 73.2 and 76.5 eV) along with a very low-intensity doublet for Pt⁺⁴ (Fig. 3a) [50]. The Pt 4f 7/2 binding energy peak in Pt₁-HCN samples, Pt₁-HCN (0.38%)–125 and Pt₁-HCN(0.75%)–125 was located at around 73.0 eV, indicating Pt⁺² as the principal ionic Pt species, Fig. 3b and c. The relative fraction of Pt⁺² in the sample with 0.38 wt% Pt was about 93%, and it decreased to around 67% when the Pt content rose to 0.75 wt%, Table S4.

By increasing the Pt loading, Pt_{mix}-HCN (1.5%)–125 and Pt_{mix}-HCN (3.5%)–125, the dominant peak relocated to 75.0 eV, exhibiting the superiority of Pt⁺⁴ (Fig. 3d and e, Table S4). Accordingly, we inferred that the oxidation state of most Pt was close to +2 in low-loading Pt-

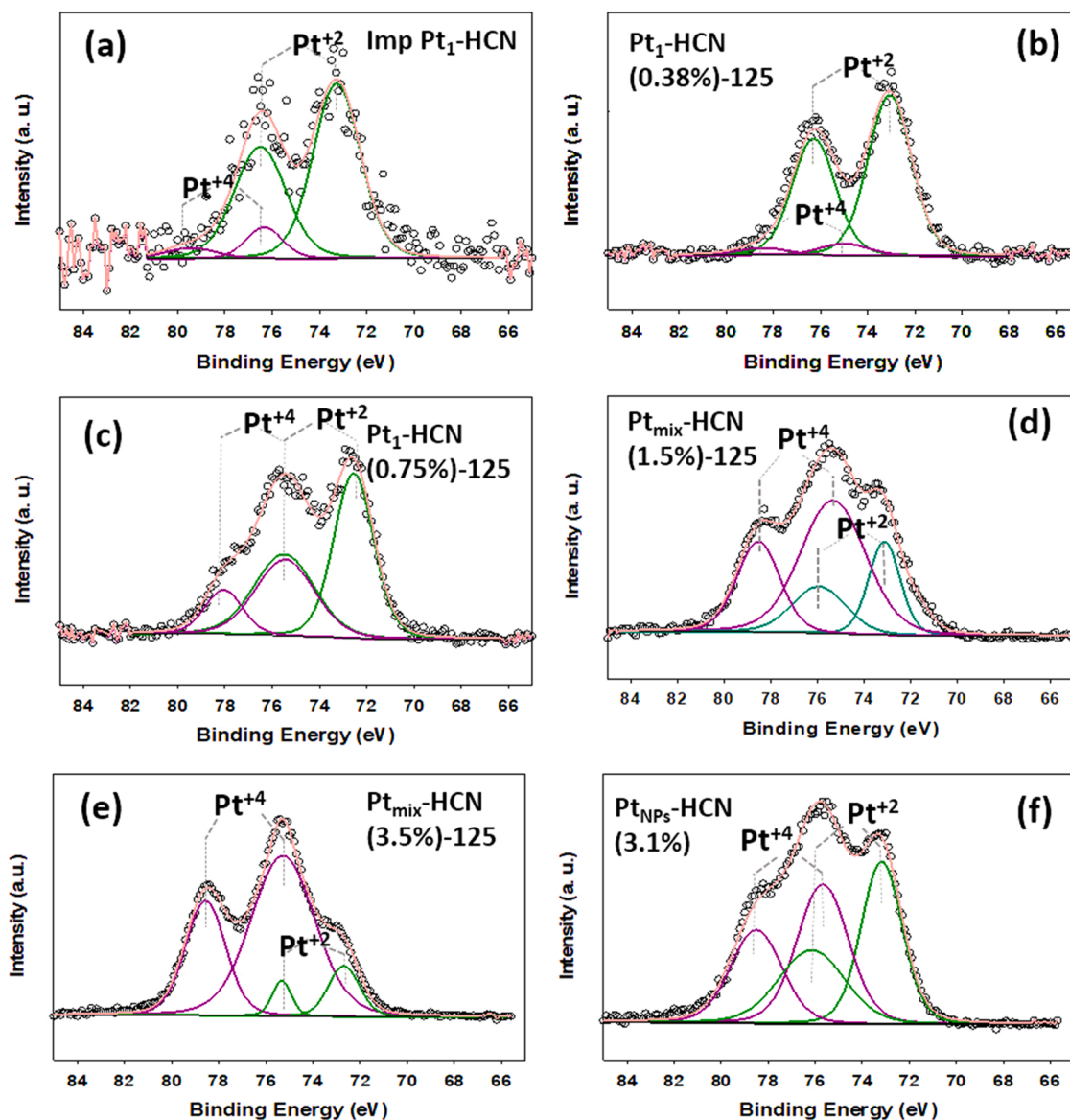


Fig. 3. Deconvoluted Pt 4f XPS spectra of (a) Imp Pt₁-HCN, (b) Pt₁-HCN (0.38%)–125, (c) Pt₁-HCN (0.75%)–125, (d) Pt_{mix}-HCN (1.5%)–125, (e) Pt_{mix}-HCN (3.5%)–125, and (f) Pt_{NPs}-HCN (3.1%).

HCN samples calcinated at 125 °C. In contrast, the oxidation state is mainly close to + 4 in highly loaded Pt samples.

As thermal activation (annealing) temperature increased from 125 to 325 °C, the relative fraction of Pt^{+2} showed the same value of about 90% for all Pt_x -HCN catalysts (Fig. S12, and Table S5). The Pt 4 $f_{7/2}$ peak position also demonstrated a negative shift, which can be attributed to the partial reduction of Pt oxidation states. Thus, the Pt oxidation state will be less than + 2 for samples that are calcinated at 325 °C.

The Pt 4 f XPS data for the bulk samples are presented in supplementary Fig. S13. The results confirmed the oxidation state of close to + 4 for the bulk samples. Besides, a mixture of Pt^{+2} and Pt^{+4} was obtained for Pt_{NPS} -HCN, Fig. 3f, and Table S4.

The electronic state and local structure of absorbing Pt atoms in the catalysts was explored using X-ray absorption spectroscopy (XAS). The XANES spectrum of $\text{H}_2\text{PtCl}_6 \bullet 6 \text{H}_2\text{O}$ (Fig. 4a) showed an absorption edge (white line (WL) peak) at 11,568 eV. It also depicted an additional peak belonging to Pt-Cl at 11,580, which is indexed to the hybridization of Pt 5d and Cl 3d in the H_2PtCl_6 structure [18]. The second peak at 11,580 eV was not detectable for the Imp Pt_1 -HCN and Imp Pt_1 -BCN samples (Fig. 4a, and b). Nevertheless, the WL peak position also shifted to higher energy compared to pure H_2PtCl_6 (inset of Fig. 4a and b). This positive shift in binding energy demonstrated the successful process of ligand exchange of chloride to nitrogen for Pt centers during the impregnation process [17,51]. The electronegativity of chlorine and nitrogen are equal, but the partial negative charge acquired on the Cl is distributed all over the larger chlorine atom. Because the charge density is reduced, it cannot attract a partial positive charge on the Pt, like nitrogen with a higher charge density. Hence, the Pt centers experience a higher positive charge in the presence of nitrogen ligands in Imp Pt_1 -HCN and Imp Pt_1 -BCN compared to that of Pt in $\text{H}_2\text{PtCl}_6 \bullet 6 \text{H}_2\text{O}$, which leads to higher required absorption energy for electron excitation and a positive shift in WL peak position.

The WL peak appeared at almost the same binding energy as the impregnated samples upon annealing of impregnated supports for Pt_1 -HCN (0.75%)–125 and Pt_1 -BCN(0.75%)–125. After annealing at 325 °C, Pt_1 -HCN (0.75%)–325 showed a WL peak with a considerable negative shift to lower binding energy (Fig. 4a). This can be attributed to the reduction of the Pt oxidation state, which was also confirmed with Pt 4 f XPS results.

For the XANES curve at the Pt L₃-edge, the intensity of the white line peak is proportional to the population of unoccupied Pt 5d [52,53]. For the prepared and reference samples the white line intensity decreased in the order of Pt_{mix} -HCN (1.5%)–125, Imp Pt_1 -BCN, Pt_1 -BCN (0.75%)–125 > H_2PtCl_6 > Pt_1 -HCN (0.75%)–125 > Pt_{NPS} -HCN > Imp Pt_1 -HCN > Pt_1 -HCN (0.75%)–325 > Pt foil, which is consistent with the trends in oxidation state acquired from XPS measurements.

Based on the obtained data for Pt charge states from XPS and XANES and the zeta potential values for HCN and BCN, we can conclude that the HCN support interacted more efficiently with Pt_1 sites compared to BCN and stabilized them by partial reduction of the Pt^{+4} ions to Pt^{+2} during the impregnation process (Table S6). Hence, HCN provided stronger adsorption sites for the Pt species through effective charge transfer compared to the BCN. These strong electronic interactions will facilitate charge separation and transfer in the catalyst structure and also protect single isolated Pt sites from sintering during the annealing process. In general, we can say HCN has redox mediating behavior that can directly affect the electronic interactions at the metal-support interface.

The local structure of the Pt_1 – N_x species and their formation were investigated using extended X-ray absorption fine structure spectroscopy, EXAFS. The k^2 -weighted Pt L₃-edge EXAFS spectra for the Imp Pt_1 -BCN and Imp Pt_1 -HCN, Fig. 5a and c, showed a prominent evolved peak that can be assigned to the Pt-N or Pt-C scattering at around 1.50 Å for HCN and 1.60 Å for BCN, which was different from the Pt-Cl in pure $\text{H}_2\text{PtCl}_6 \bullet 6 \text{H}_2\text{O}$ around 2.0 Å and Pt-Pt in Pt foil at 2.4 Å. It is noteworthy to consider that EXAFS cannot differentiate C, N, and O as the different coordinated sites due to their similar scattering parameters as a result of their neighboring positions in the periodic table of elements [13]. Even so, we determined that the exchanged ligands instead of Cl[−] for Pt in HCN and BCN structures are nitrogen atoms (not carbon atoms) based on the positive shift of WL peak for the samples compared to H_2PtCl_6 in XANES spectra and higher electronegativity of nitrogen compared to carbon. In addition, the smaller bonding distance of Pt-N in Imp Pt_1 -HCN (around 1.5 Å) revealed the formation of stronger electronic interactions between Pt_1 and HCN during the impregnation process than that of Pt_1 and BCN (about 1.6 Å). After annealing at 125 °C, the Pt-N bond showed the same length of around 1.62 Å for both Pt_1 -HCN (0.75%)–125 and Pt_1 -BCN (0.75%)–125.

All of the prepared catalysts showed a second peak at 2.6 Å due to Pt-C scattering (second coordination shell). Fig. 5a and c [13,18] prove that ionic Pt species in nitrogen pores have electronic interactions with carbon atoms in heptazine rings. Thermal activation treatment (annealing) of impregnated samples at 125 °C did not change the scattering peak positions Pt-N and Pt-C. A significant intensity decrease in the Pt-N peak after increasing the annealing temperature to 325 °C suggests a noticeable drop in Pt_1 site concentrations in the Pt_1 -HCN (0.75%)–325 (Fig. S14).

For the Pt_{NPS} -HCN sample, a clear intense peak at around 1.6 Å can be assigned to Pt-O scattering, Fig. 5a. This is in agreement with the XRD result that proves the formation of PtO nanoparticles. No peaks of Pt–Pt scattering (observed at 2.6 Å for Pt foil) were detected for Pt_{NPS} -HCN.

EXAFS fitting was performed to analyze the structural parameters of Pt atoms in HCN and BCN structures. The fitted parameters are reported

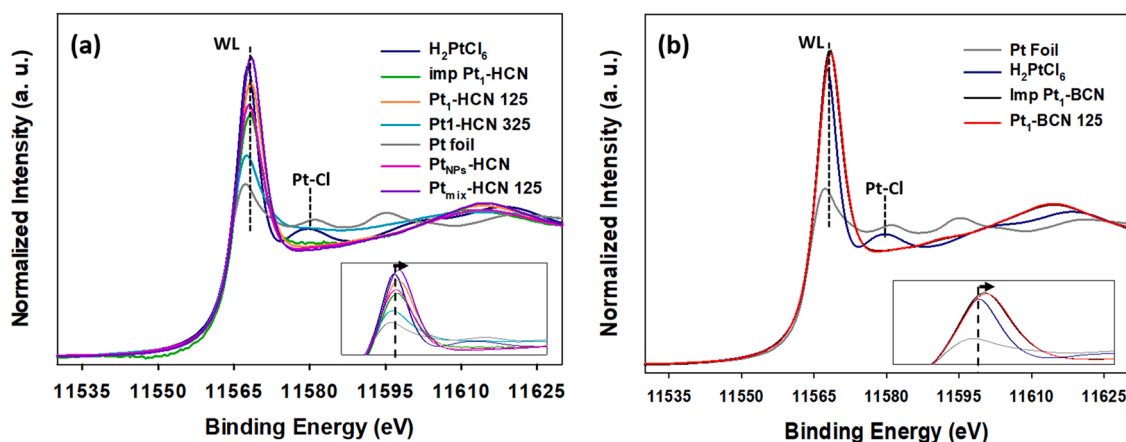


Fig. 4. Pt L₃-edge XANES spectra for (a) Imp Pt_1 -HCN, Pt_1 -HCN (0.75%)–125, Pt_1 -HCN (0.75%)–325, Pt_{mix} -HCN (1.5%)–125, and Pt_{NPS} -HCN (3.1%), Pt foil, pure H_2PtCl_6 and (b) Imp Pt_1 -BCN, Pt_1 -BCN (0.75%)–125, Pt foil, pure H_2PtCl_6 . The insets show the corresponding magnified white lines.

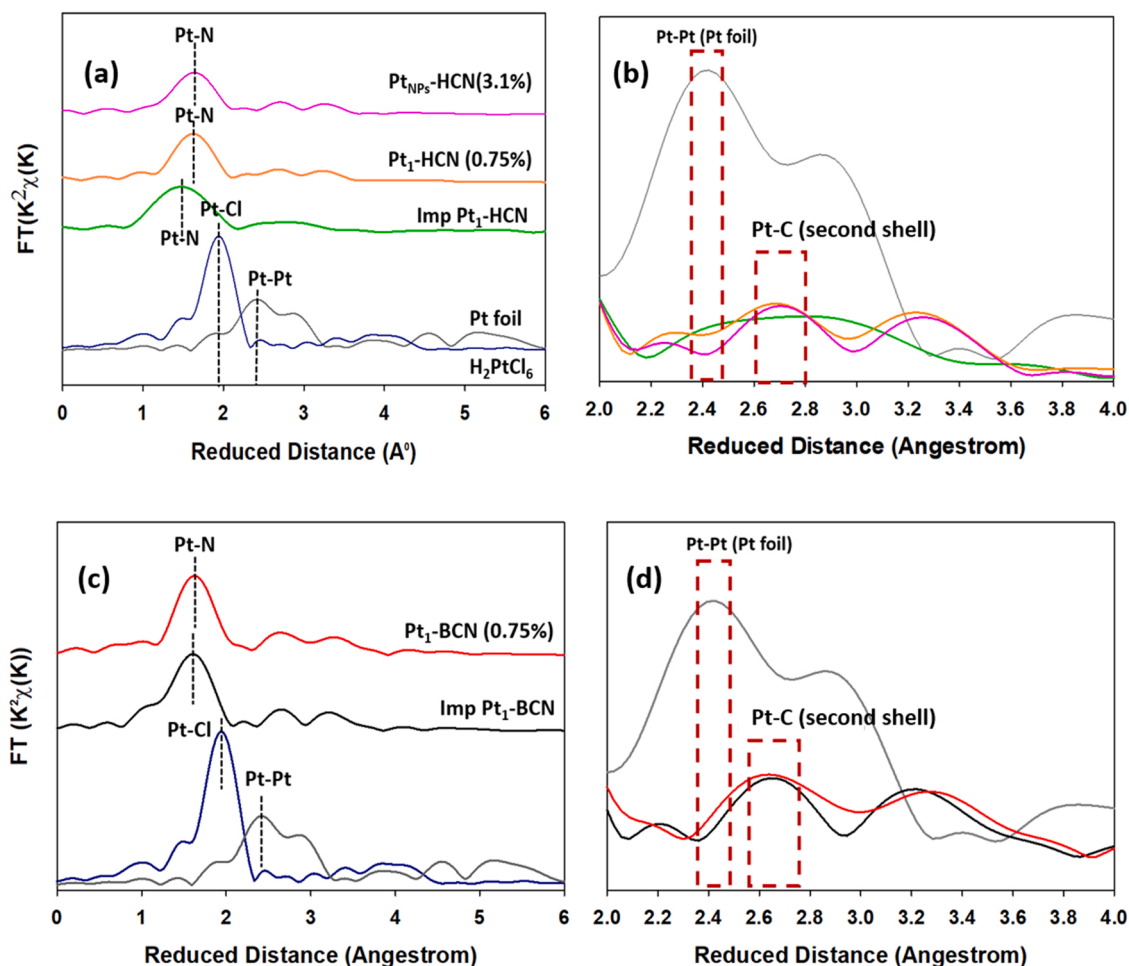


Fig. 5. Fourier transform-EXAFS spectra of (a) Imp Pt-HCN, Pt₁-HCN (0.75%)–125, and Pt_{NPS}-HCN (3.1%), Pt foil, and pure H₂PtCl₆, and (b) the corresponding magnified second shell scattering for Pt-C interactions, and the absence of Pt-Pt interactions in Pt-HCN samples. Fourier transform-EXAFS spectra of (c) Imp Pt-BCN, Pt₁-BCN (0.75%)–125, Pt foil, and pure H₂PtCl₆, and (d) the corresponding magnified second shell scattering for Pt-C interactions and the absence of Pt-Pt interactions in Pt₁-BCN.

in Table S6. Interestingly, the Pt-isolated sites (Pt₁) have been coordinated with different coordination numbers (CN) in BCN and HCN. The average coordination number for Pt₁-BCN (0.75%)–125 is 5.7, which shows the presence of CN = 6 and CN = 5. This confirms that most Pt₁⁴⁺ ions in BCN are fully coordinated with six nitrogen atoms, Pt⁴⁺-N₆. Still, fewer Pt₁⁴⁺ coordinated with five nitrogen atoms and constructed Pt⁴⁺-N₅ moieties.

The average coordination number for Pt₁-HCN (0.75%)–125 is 4.3, indicating the prominent Pt²⁺-N₄ moieties formation alongside fewer Pt⁴⁺-N₅ ones. Apart from this, the fitting result for Pt₁-HCN (0.75%)–325 showed a decrease in coordination number to 3.4 as well.

3.2. Electronic interactions between Pt single atoms and different g-C₃N₄ structures as supports

The goal of electronic metal support interactions (EMSIs) is to balance the d-band orbitals of active metal sites through the charge transfer between supports and metal atoms. Thus, the oxidation state of the metal single atoms on the support is entirely controlled by the electronic metal-support interactions. The EXAFS fitting data combined with XANES and Pt4f XPS results accompanied by zeta potential values reinforced the hypothesis that the HCN support plays a key role in the stabilization of Pt²⁺ at low loading Pt < 1 wt% (through higher charge transfer ability and reduction of Pt⁴⁺ to Pt²⁺ during the impregnation process). At the lowest Pt loading value of 0.38 wt%, almost 93% of Pt⁴⁺

was reduced to Pt²⁺. By increasing the loading amount to 0.75 wt%, the Pt²⁺ relative fraction shrunk to 67% based on Pt 4f XPS results.

Stabilized Pt²⁺ centers on HCN facilitated the formation of unsaturated coordinated Pt²⁺-N₄ moieties after the thermal activation process at 125 °C. Nevertheless, BCN did not form enough electronic interactions with Pt⁴⁺ centers to reduce them to Pt²⁺ sites. Hence, due to the higher charge state of Pt⁴⁺, the formation of fully coordinated Pt⁴⁺ centers was stimulated compared to unsaturated ones.

XPS and XANES results for samples with higher Pt loadings on HCN displayed that HCN did not reduce Pt⁴⁺ species effectively, and most of the Pt⁴⁺ centers remain unchanged. Some theoretical calculations have demonstrated the presence of preferred sites for single atomic metals. When, there is a low metal loading, mostly thermodynamically stable sites are occupied with ionic metals. But by increasing the metal content and the lack of the vacancy of thermodynamically stable sites, the extra atoms are kinetically trapped in metastable positions. It seems that metastable sites did not electronically interact with Pt single atoms as was observed for HCN at Pt loadings > 1 wt%. Also, the formation of kinetically metastable Pt sites increased the chance of sintering atomic sites during the annealing step, as was confirmed by HAADF-STEM images for Pt_{mix}-HCN (1.5%)–125, Fig. S7.

Upon increasing the thermal activation (annealing) temperature to 325 °C in Pt₁-HCN (0.75%)–325, the coordination number drops from 4 to 3, confirming the local geometry change for the remaining Pt₁ active sites. The coordination number reduction is plausible, as previous XPS

and XANES results also implied a decrease in the + 2 Pt charge state after calcination at 325 °C.

3.3. Effect of Pt₁ sites and Pt_{NPs} on optical and electrochemical properties

The optical properties of bulk and hexagonal g-C₃N₄ were thoroughly explored in our previous work. The results proved that moving from the bulk to the hexagonal nanosheet structure improves the optical and electronic properties in the g-C₃N₄ framework as a photocatalyst. Herein, we endeavored to evaluate the effect of Pt loading in the form of single atoms and nanoparticles on the optical and electronic properties of HCN. As shown in Fig. 6a, the light absorption spectrum of HCN consists of a strong intrinsic absorption band with an edge at about 430 nm, corresponding to a bandgap of about 2.9 eV. However, the introduction of Pt atoms leads to the appearance of a very weak absorption band starting from the edge and ending around 600 nm without any change in the intrinsic band gap, Fig. 6b-e. The weak absorption peak gets stronger by increasing Pt loading in the structure from 0.38 wt % to 3.5 wt%. The first (stronger) absorption band is caused by the excitation of the electrons from the valence band to the conduction band of HCN, and the second (weaker) one is related to excitations from the valence bands to the localized states, which originate from the Pt energy states. Considering the negligible difference in UV-Vis absorption spectra of HCN and Pt₁-HCN and the corresponding acquired band gap values, Fig. 6b-e, the existing Pt₁ localized states did not effectively promote the light-harvesting ability of HCN.

Charge separation and recombination were examined using steady-state photoluminescence spectroscopy, and the PL spectra of pure HCN and BCN are illustrated in Fig. 7a. The charge recombination has been effectively reduced in HCN structure compared to BCN. Pt deposition at low concentrations in Pt₁-HCN (0.38%) and Pt₁-HCN (0.75%) caused more efficient suppression of radiative electron-hole recombination compared to Pt nanoparticles as shown by the weaker intensity of PL peaks, Fig. 7b. Time-resolved photoluminescence (TRPL) spectroscopy was conducted at the emission wavelength of each sample to explore the charge carrier dynamics. The results demonstrated the gradual shortening of PL lifetime with increasing Pt content (Table S7). Shorter PL lifetimes in the samples are linked to the presence of Pt sites, which provide electron trapping states to accept photoexcited electrons and suppress radiative recombinations, improving photocatalytic

activity. Pt atoms introduce 5d orbitals into the g-C₃N₄ band gap. Then, the Pt d orbitals split in the valence band and conduction band based on metal support electronic interactions and restructure the electronic format g-C₃N₄ by changing the valence band and conduction band position, Fig. 7e. The photogenerated electrons transfer from the conduction band of HCN to the Pt atoms orbitals and participate in the H₂ evolution reaction [26]. Based on the optical properties, we concluded that the presence of Pt₁ as the co-catalyst effectively suppresses radiative charge recombinations and provides a more efficient electron/hole separation and transfer in the structure.

The electrochemical properties of the prepared photocatalysts were examined using electrochemical impedance spectroscopy (EIS). The Nyquist plot data for all samples were fitted with an equivalent electrical circuit (Randle model) to assess the charge transfer resistance (R_{ct}) at the electrode/electrolyte interfaces and double-layer capacitance properties (Table S8). The R_{ct} showed considerable reduction after Pt deposition on HCN for both Pt_{NPs} and Pt₁ sites. Based on the R_{ct} values, Table S9, and the semicircle diameter of Nyquist plots (Fig. 7c), Pt₁ can successfully decrease the charge transfer barrier at the electrode/electrolyte interface and facilitate water reduction reaction nearly as effectively as Pt_{NPs}.

The electrochemical active surface area (ECSA), which is normally proportional to the double-layer capacitance (C_{dl}) of the catalysts, was investigated by fitting results in Nyquist plots, Table S8. The C_{dl} value increased dramatically in the presence of Pt₁ on HCN. Interestingly, the same C_{dl} was obtained for the Pt_{NPs} and Pt₁, which showed a similar available electrochemical active surface area for the hydrogen evolution reaction, which is much greater than that of pristine HCN.

3.4. Photocatalytic hydrogen evolution

The photocatalytic hydrogen evolution (PHE) of the prepared photocatalysts was examined in a 20% aqueous solution of triethanolamine using a 250 mL photoreactor, which was irradiated from above with a 300 W xenon lamp without the addition of any photosensitizer. As shown in Fig. 8a, a total rate of 2900 μmol g⁻¹ h⁻¹ was generated on Pt₁-HCN- (0.38%)– 125 at 10 °C. This value was around 518 μmol g⁻¹ h⁻¹ on Pt₁-BCN (0.38%)– 125. The acquired values in the case of Pt_{NPs}-HCN and Pt_{NPs}-BCN were 1400 μmol g⁻¹ h⁻¹ and 186.0, respectively. The photocatalytic hydrogen evolution rate in HCN increased by almost 2.0

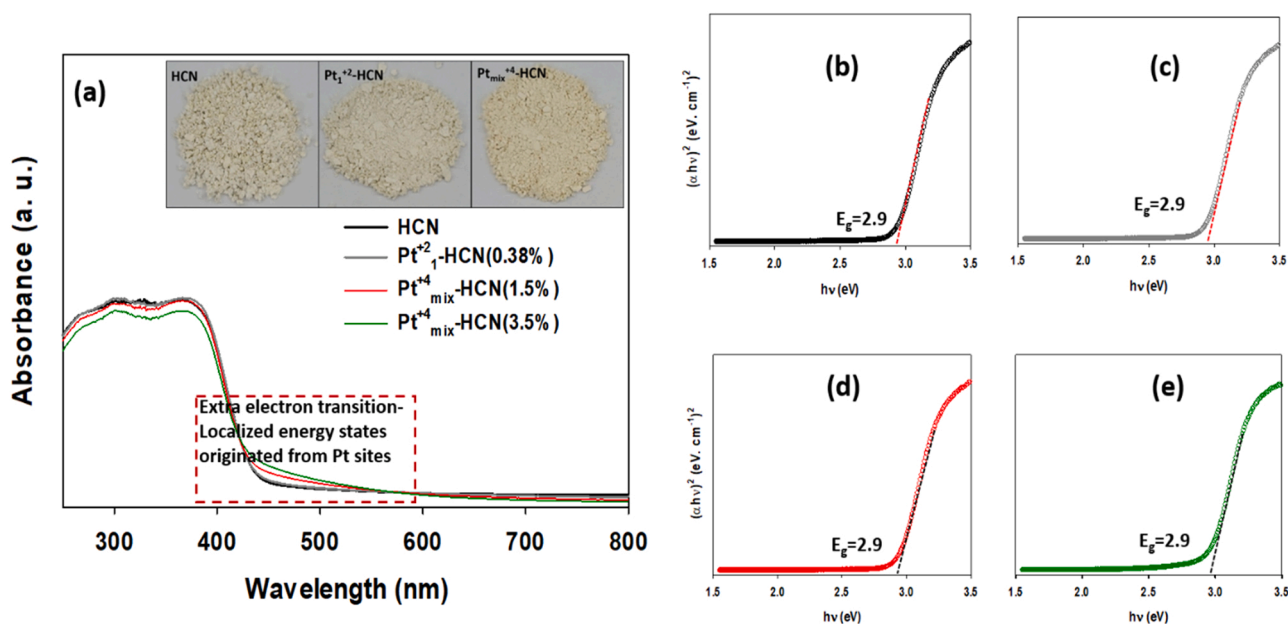


Fig. 6. (a) UV-Vis absorption spectra of HCN, Pt₁-HCN (0.38%)– 125, Pt_{mix}-HCN (1.5%)– 125, and Pt_{mix}-HCN (3.5%)– 125, (b) Corresponding Tauc plots for band gap estimation of HCN, Pt₁-HCN (0.38%)– 125, Pt_{mix}-HCN (1.5%)– 125, and Pt_{mix}-HCN (3.5%)– 125.

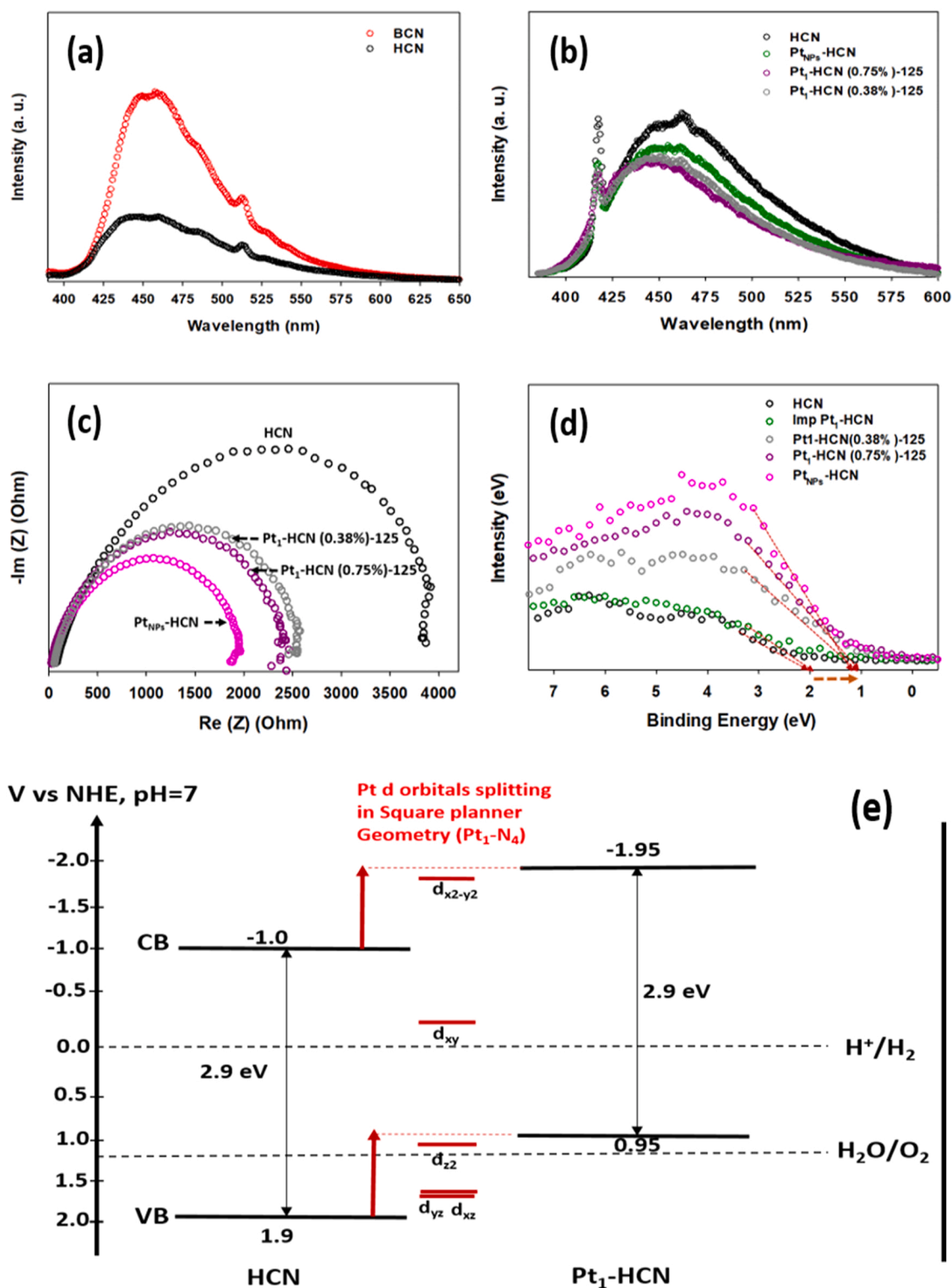


Fig. 7. Steady-state PL spectra of (a) BCN and HCN, (b) HCN, Pt_{NPs}-HCN, Pt₁-HCN (0.38%)-125, and Pt₁-HCN(0.75%)-125, (c) EIS spectra of HCN, Pt_{NPs}-HCN, Pt₁-HCN (0.38%)-125, and Pt₁-HCN(0.75%)-125, (d) XPS valence band measurements for HCN, Pt_{NPs}-HCN, Imp Pt₁-HCN Pt₁-HCN (0.38%)-125, and Pt₁-HCN (0.75%)-125, (e) Electronic band structure of HCN and Pt₁-HCN (how the Pt d orbitals restructure the electronic band structure in HCN).

times based on the support weight by decreasing the total amount of deposited Pt from 3.1 wt% in nanoparticles to 0.38 wt% in single atomic sites (8.1 times lower Pt percentage).

In addition to acting as co-catalysts, Pt₁ sites act as the reactive sites in photocatalytic H₂ evolution as well. The electrochemical impedance spectroscopy (EIS), electrochemical surface area measurements, steady-

state, and time-resolved photoluminescence (TRPL) spectroscopy results proved that the photoexcited electrons transferred from the bulk to the surface and finally captured by the Pt sites where the H₂O adsorption, H₂O dissociation, and H₂ evolution take place. In Fig. 8b, the photocatalytic H₂ production is reported based on the Pt content as active sites (Mass activity for Pt). As shown, the PHE activity of the Pt₁ on the HCN

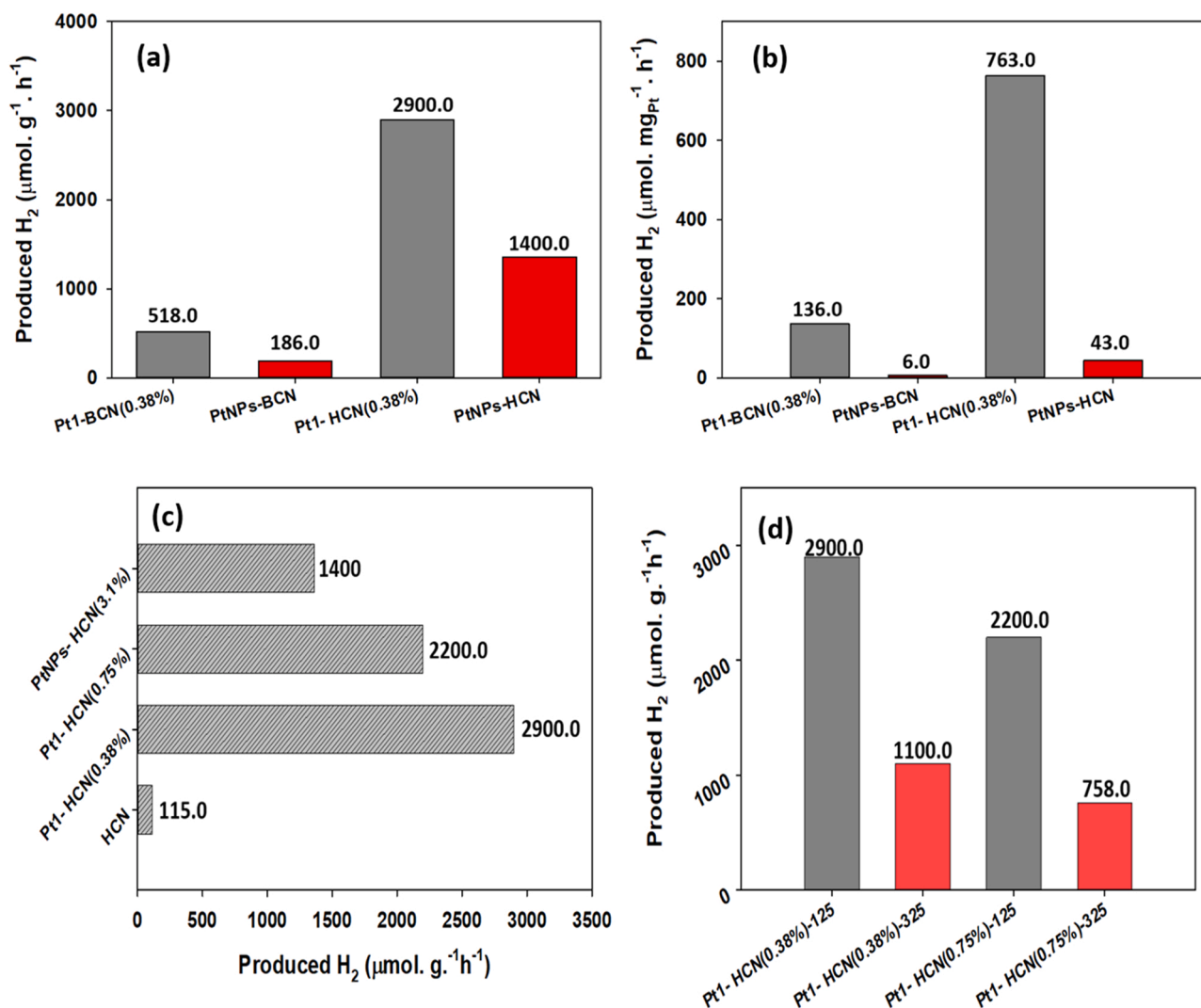


Fig. 8. Photocatalytic performance of pristine and Pt-deposited HCN and BCN samples toward H₂ production. (a) H₂ evolution performance of HCN, Pt₁-HCN-125, PtNPs-HCN, BCN, Pt₁-BCN-125, PtNPs-BCN (b) H₂ generation performance of Pt-HCN samples with various Pt values normalized per 1 mg of Pt (the Pt mass activity). (c) Comparison of H₂ evolution performance on HCN with different Pt loading (isolated sites and nanoparticles) (d) H₂ evolution performance of Pt₁-HCN samples at different thermal activation temperatures.

showed the highest value compared to others. The Pt₁-HCN-(0.38%)–125 produced 763 μmol mg_{Pt}⁻¹ h⁻¹, which is 17.7 times higher than that of Pt active sites on PtNPs-HCN-(3.1%) and 5.6 times higher than Pt₁ sites on Pt₁-BCN (0.38%)–125.

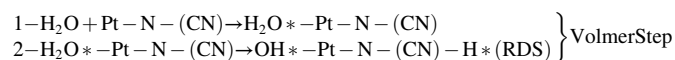
The influence of Pt loading and annealing temperature on the PHE of Pt₁-HCN photocatalysts was also studied. Fig. 8c compares the effect of the Pt loading amount on photocatalytic H₂ production in the HCN structure. By increasing the Pt loading amount in Pt₁-HCN photocatalysts from 0.38 wt% to 0.75 wt%, a noticeable PHE drop from 2900 to 2200 μmol g⁻¹ h⁻¹ was observed. Also, Fig. 8d indicates the effect of annealing temperature in PHE Pt₁-HCN photocatalysts. The photocatalytic activity after thermal activation at the higher temperature of 325 °C dramatically decreased showing a hydrogen evolution rate of 1100 and 758 μmol g⁻¹ h⁻¹ for Pt₁-HCN (0.38%)–325, and Pt₁-HCN (0.75%)–325.

To evaluate the intrinsic activity of Pt₁ on HCN we estimated the turnover frequency (TOF), which indicates the activity of a catalyst on a per-Pt-active site. For the calculation of TOFs, all Pt sites at the catalyst surface were treated as active sites for hydrogen evolution reaction based on the Pt content measurements by ICP-OES analysis. The TOF of Pt₁-HCN with 0.38 wt% Pt loading reaches 149 h⁻¹ which is about 17 times higher than that of the TOF of PtNPs-HCN (TOF= 8.8 h⁻¹) with

3.1 wt% Pt loading. The calculated TOF for other prepared catalysts was reported in Fig. S15a. Also, the stable hydrogen production of the Pt₁-HCN for 24 h indicated the stability of the photocatalyst under working conditions, Fig. S15b.

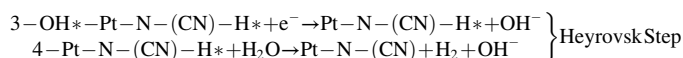
3.5. Theoretical investigation of HER activity on Pt⁺² and Pt⁺⁴

To further understand the origin of PHE activities on Pt₁⁺²-g-C₃N₄ and Pt₁⁺⁴-g-C₃N₄, a theoretical investigation based on DFT calculations was conducted, and water adsorption, dissociation, and H^{*} adsorption were calculated. The PHE in an alkaline environment is initiated by water adsorption on the active sites (here Pt species), Step (1), and then it is followed by water dissociation to adsorbed OH^{*} on Pt and H^{*} on N, Step (2) (Step 1 and Step 2 constitute the Volmer step). The water dissociation in Step (2) has sluggish kinetics, making it the rate-determining step (RDS):



After, the formation of H^{*} and OH^{*} at the catalytic sites, the reaction continues with a Heyrovsky step in which the molecular H₂ will be

released by the interaction of H^* with H_2O through two steps:



First, water adsorption energy on Pt^{+2} and Pt^{+4} was considered. The H_2O molecule has larger adsorption energy of -2.10 eV on Pt^{+4} compared to -0.61 eV on Pt^{+2} . The kinetics of water dissociation into the H^* and OH^* corresponding to Step (2) were also computed. Fig. 9a shows that the kinetic energy barrier for the Volmer step on Pt^{2+} -g- C_3N_4 is 0.17 eV , which is three times lower than that of Pt^{4+} -g- C_3N_4 , 0.51 eV . Furthermore, the exothermic process of -0.56 eV on Pt^{+2} with an endothermic process (0.05 eV) on Pt^{+4} indicates a much easier dissociation of H_2O in alkaline conditions [54]. This theoretical trend agreed well with the experimental observation, confirming the outstanding HER performance of the Pt^{+2} -g- C_3N_4 system.

We calculated the free energy profile and H adsorption, ΔG_{H^*} , using density functional theory as shown in Fig. 9b.

The free energy of hydrogen adsorption over a catalytic surface is a well-known descriptor to evaluate the hydrogen evolution reaction (HER) performance of catalysts [55]. The kinetic barrier of the HER mechanism was computed using the climbing image nudged elastic band approach (CI-NEB) [56]. The lower free energy of Pt^{+2} -g- C_3N_4 than that of Pt^{+4} -g- C_3N_4 reveals that it is a better catalyst for HER. Moreover, the ΔG_{H^*} value for the Pt^{+2} -g- C_3N_4 is approaching the free energy of $Pt(111)$ (0.09 eV) [55].

3.6. Structure and performance relationship

The zeta potential measurement results for HCN and BCN associated with Pt 4 f XPS confirmed the reduction of adsorbed Pt^{+4} to Pt^{+2} during the impregnation process at low Pt loading values on HCN. The Pt 4 f XPS data showed that the relative fraction of Pt^{+2} decreased from 96% to 67% by increasing the Pt loading from 0.38 wt% to 0.75 wt%. For a higher Pt loading of $> 1\text{ wt\%}$, this value decreased to 36%. Further, HAADF-STEM images confirmed the formation of Pt clusters and nanoparticles. Hence, the Pt_1 sites are only formed for Pt loadings under 1 wt\% . The obvious reduction of Pt^{+2} percentage by increasing loading from 0.38 wt% to 0.75 wt% suggests the presence of diverse Pt coordination environments in the HCN structure. At the lowest Pt loading of 0.38 wt%, almost all thermodynamically favorable coordination sites were occupied with Pt ionic species and the favorable electronic interactions provided a reduction of 93% deposited Pt^{+4} ($H_2PtCl_6 \cdot H_2O$) to Pt^{+2} . The Pt^{+2} coordination number in Imp Pt_1 -HCN was around six, after annealing at 125°C due to the d^8 electron configuration of Pt^{+2} ,

which facilitates the formation of a square planar geometry. Even so, the coordination number dropped to 4 to stabilize Pt_1 geometry in a HCN structure. Increasing Pt loading to 0.75 wt% caused a visible reduction of the Pt^{+2} to 67% and the remaining Pt species (33%) retained an ionic charge of $+4$. The average coordination number of 4.3 signifies the existence of two distinct Pt_1 coordinating environments on HCN. The 4.3 coordination number shows the possibility of $CN=5$ and $CN=4$ for Pt^{+4} and Pt^{+2} species, respectively. This means that increasing Pt loading caused extra Pt atoms to coordinate on kinetically metastable sites where electronic interactions are not sufficient to reduce Pt^{+4} to Pt^{+2} . Consequently, the Pt^{+2} species coordinate with 4 nitrogen, and the Pt^{+4} species coordinate with 5 nitrogen atoms. Hence, the average ratio of $CN=4$ and $CN=5$ is 67/33.

The PHE measurements indicated that Pt_1 -HCN (0.38%)–125 has a higher activity of $2900\text{ }\mu\text{mol g}^{-1}\text{ h}^{-1}$ compared to Pt_1 -HCN (0.75%)–125 with an activity of $2200\text{ }\mu\text{mol g}^{-1}\text{ h}^{-1}$. This enhancement in the PHE rate for Pt_1 -HCN (0.38%)–125 is a result of the almost uniform formation of 93% unsaturated Pt^{+2} - N_4 , which makes electronically active and sterically unhindered Pt_1 - N_4 sites. However, the PHE activity decreased due to the presence of around 33% of Pt^{+4} - N_5 on Pt_1 -HCN (0.75%)–125. This proves that the 4 coordinated Pt^{+2} is the most active coordination site on HCN as DFT calculations of water dissociation and H^* adsorption in the previous section exhibited that Pt^{+2} is a more favorable site for water reduction compared to Pt^{+4} . Moreover, the four coordinated environments of Pt^{+2} provide higher accessibility of water molecules to adsorb on Pt sites due to the steric effect.

The electronic and steric parameters were worse in Pt_1 -BCN catalysts because Pt^{+4} has a higher kinetic barrier for water dissociation and higher H^* adsorption energy than all other Pt species. Indeed, the Pt^{+4} species showing low activity for water reduction are mostly coordinated with 6 nitrogen rather than 5. A coordination number six for the less active Pt^{+4} destroys reactivity as its fully coordinated environment stops the adsorption of water molecules both electronically and sterically. In this case, Pt^{+4} - N_5 will be the reactive species due to their unsaturated geometry, which is much less reactive compared to Pt^{+2} - N_4 on HCN. Fig. 10a and b schematically demonstrate the formation and reactivity of Pt^{+2} - N_4 on hexagonal g- C_3N_4 and Pt^{+4} - N_5 on bulk g- C_3N_4 .

It is worth mentioning that Pt^{+2} - N_4 sites (due to their unsaturated coordinative nature) are similar to metalloenzymes, which actively participate in multiple water molecule adsorption and dissociation by easily changing their structural configurations and valence states Table 1.

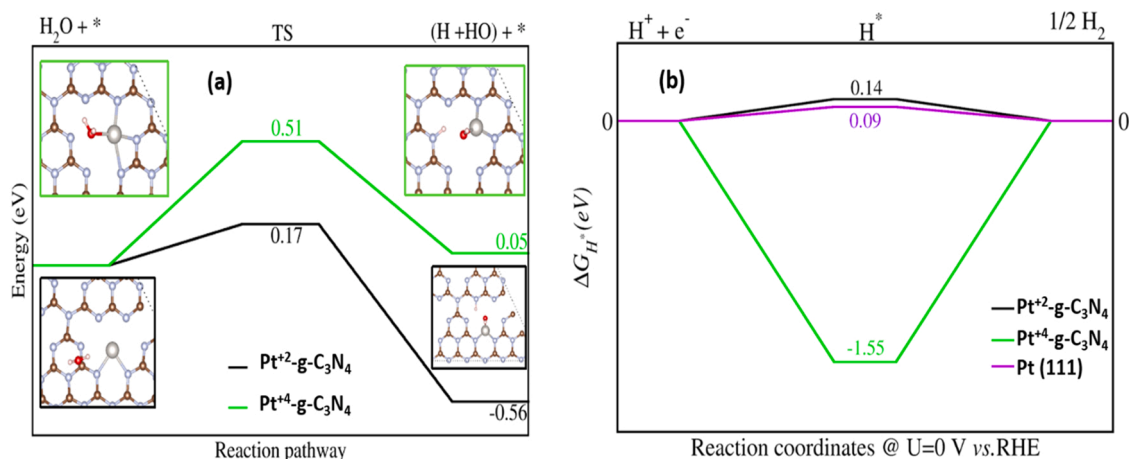


Fig. 9. (a) Reaction pathway for the H_2O dissociation over Pt^{+2} -g- C_3N_4 and Pt^{+4} -g- C_3N_4 catalysts. (b) Free energy diagram profile of H^* adsorption for Pt^{+2} -g- C_3N_4 , Pt^{+4} -g- C_3N_4 , and $Pt(111)$.

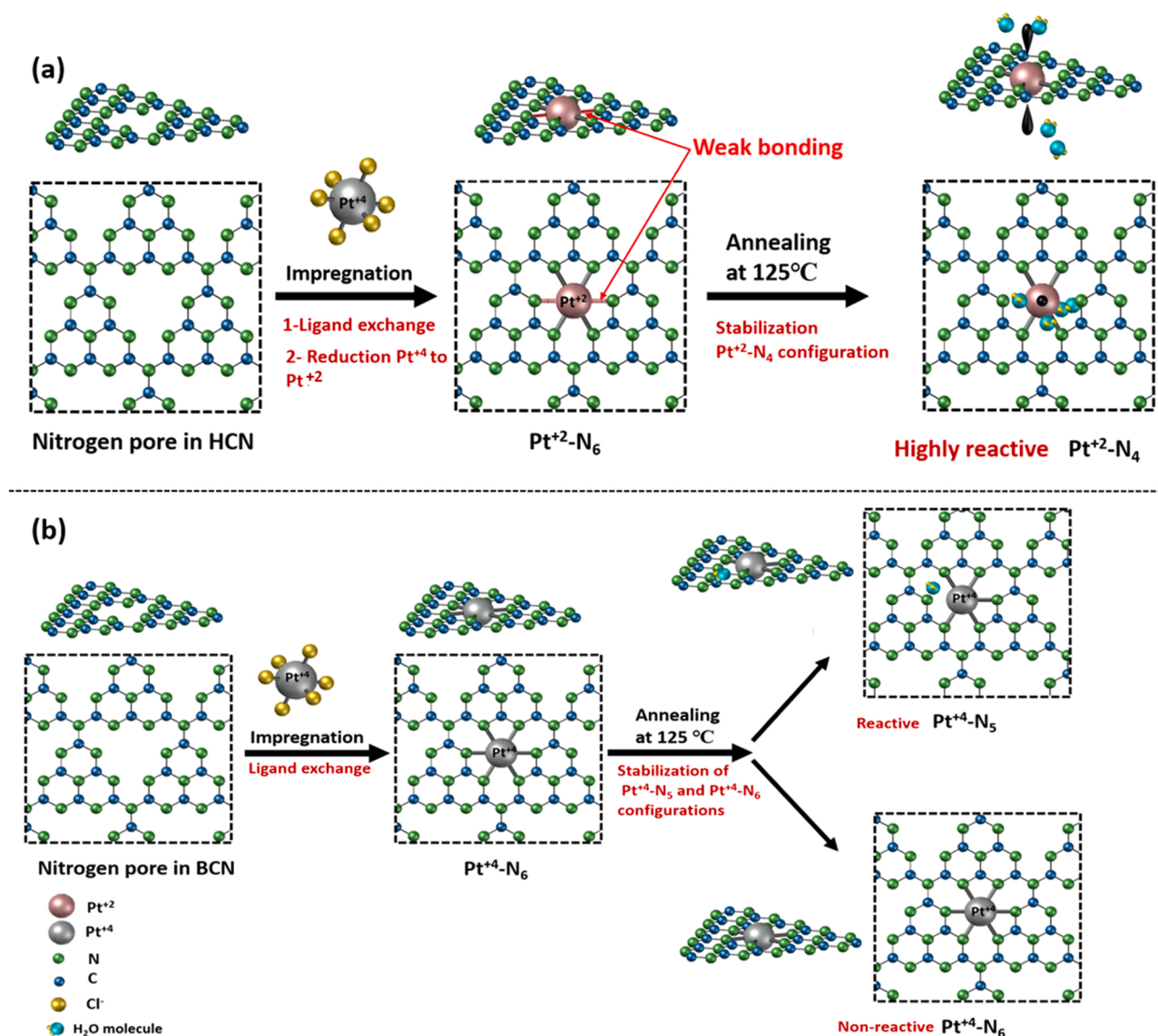


Fig. 10. The schematic diagram of the formation of (a) $Pt^{+2}-N_4$ moieties on HCN nitrogen pore and (b) $Pt^{+4}-N_6$ and $Pt^{+4}-N_5$ on BCN nitrogen pore.

4. Conclusion

In summary, we elucidated the creation of different catalytically active configurations of single atomic Pt sites on HCN and BCN by systematic investigation of the structure-sensitive XAS analysis of atomically well-dispersed Pt single atomic sites. According to the acquired results, HCN as light-sensitive support actively reduced the adsorbed Pt^{+4} ions to Pt^{+2} due to its redox mediating properties and strong electronic interactions with Pt species. Employing HCN as the support facilitated the formation of coordinatively unsaturated Pt centers ($Pt^{+2}-N_4$) to provide more favorable electroactive sites for water adsorption and dissociation by easily changing their structural configurations and valence states compared to $Pt^{+4}-N_5$, and $Pt^{+4}-N_6$ sites generated on BCN. DFT calculations supported the experimental data to reveal the high-active Pt₁ sites on HCN, better water adsorption and dissociation of Pt^{+2} site, and enhancing HER by reducing H^* adsorption energy. Deactivation of isolated Pt centers at a higher thermal activation temperature was also observed as a consequence of decreasing the Pt oxidation state. Hence, in addition to increased accessible active sites for Pt₁, the loading mass, charge states, local coordination, and uniformity of the sites had a strong impact on their chemical reactivity and catalytic performance. Our work validates the critical role of a redox mediating

support material with the creation of uniform, electronically favorable, and stable coordination environments.

CRediT authorship contribution statement

Tahereh Mahvelati-Shamsabadi: Conceptualization, Methodology, Experiment design, Data acquisition and curation, Validation, Formal analysis, Investigation, Writing - original draft preparation, review & editing. **Kailash Chandra Bhamu:** DFT calculation, review & editing. **Seong-hun Lee:** Conducting the XAFS analysis (data analysis, Data Fitting). **Thanh Truong Dang:** Conceptualization, Methodology, Experiment design, Data acquisition, and curation. **Vu Hoang Khoi:** Conducting the electrochemical analysis, Scheme preparation, review & editing. **Seung Hyun Hur, Won Mook Choi, and Sung Gu Kang:** Manuscript-review & editing, and Supervision. **Tae Joo Shin:** Funding acquisition, Supervision, Writing - Corrections, review & editing. **Jin Suk Chung:** Project administration, Funding acquisition, Supervision, Writing - Corrections, review & editing.

All the authors commented on the manuscript and the final version of the manuscript has been approved by them.

Table 1

The list of the prepared photocatalysts, their Pt content (wt%), and synthesis Condition.

Sample	Pt (wt %)	Synthesis Condition		
		Support	Reaction Time (h)	Annealing Temperature (°C)
Imp Pt ₁ -BCN	0.75	Bulk g-C ₃ N ₄	6	-
Pt ₁ -BCN (0.38%)–125	0.38	Bulk g-C ₃ N ₄	6	125
Pt ₁ -BCN (0.75%)–125	0.75	Bulk g-C ₃ N ₄	6	125
Imp Pt ₁ -HCN	0.75	Hexagonal g-C ₃ N ₄	6	-
Pt ₁ -HCN (0.38%)–125	0.38	Hexagonal g-C ₃ N ₄	6	125
Pt ₁ -HCN (0.75%)–125	0.75	Hexagonal g-C ₃ N ₄	6	125
Pt ₁ -HCN (0.75%)–325	0.75	Hexagonal g-C ₃ N ₄	6	325
Pt _{mix} -HCN (1.5%)–125	1.5	Hexagonal g-C ₃ N ₄	6	125
Pt _{mix} -HCN (3.5%)–125	3.5	Hexagonal g-C ₃ N ₄	6	125
Pt _{NPs} -HCN	3.1	Hexagonal g-C ₃ N ₄	6	-

Declaration of Competing Interest

The authors declare that they have no known competing financial interests or personal relationships that could have appeared to influence the work reported in this paper.

Data Availability

Data will be made available on request.

Acknowledgments

This study was supported by the National Research Foundation of Korea (NRF) grant funded by the Korea government (MSIT) (2020R1A4A4079954) and Priority Research Centers Program (MOE) (2021R1A6A1A03038858) and by the Regional Innovation Strategy (RIS) through the Ministry of Education (MOE) (2021RIS-003). Experiments at PLS-II 6D UNIST-PAL beamline were supported in part by MSIT, POSTECH, and UNIST Central Research Facilities.

Supporting Information

Supporting Information is available in Online Library or from the author.

Appendix A. Supporting information

Supplementary data associated with this article can be found in the online version at [doi:10.1016/j.apcatb.2023.122959](https://doi.org/10.1016/j.apcatb.2023.122959).

References

- Y. Li, Z. Wang, T. Xia, H. Ju, K. Zhang, R. Long, Q. Xu, C. Wang, L. Song, J. Zhu, J. Jiang, Y. Xiong, Implementing Metal-to-Ligand charge transfer in organic semiconductor for improved visible-near-infrared photocatalysis, *Adv. Mater.* 28 (2016) 6959–6965, <https://doi.org/10.1002/adma.201601960>.
- J. Yan, Y. Ji, M. Batmunkh, P. An, J. Zhang, Y. Fu, B. Jia, Y. Li, S. Liu, J. Ye, T. Ma, Breaking platinum nanoparticles to single-atomic Pt-C₄ co-catalysts for enhanced solar-to-hydrogen conversion, *Angew. Chem. Int. Ed.* 60 (2021) 2541–2547, <https://doi.org/10.1002/anie.202013206>.
- D. Kim, K.K. Sakimoto, D. Hong, P. Yang, Artificial photosynthesis for sustainable fuel and chemical production, *Angew. Chem. Int. Ed.* 54 (2015) 3259–3266, <https://doi.org/10.1002/anie.201409116>.
- Y. Jiao, Y. Zheng, M. Jaroniec, S.Z. Qiao, Design of electrocatalysts for oxygen- and hydrogen-involving energy conversion reactions, *Chem. Soc. Rev.* 44 (2015) 2060–2086, <https://doi.org/10.1039/C4CS00470A>.
- Y. Shi, Z.-R. Ma, Y.-Y. Xiao, Y.-C. Yin, W.-M. Huang, Z.-C. Huang, Y.-Z. Zheng, F.-Y. Mu, R. Huang, G.-Y. Shi, Y.-Y. Sun, X.-H. Xia, W. Chen, Electronic metal-support interaction modulates single-atom platinum catalysis for hydrogen evolution reaction, *Nat. Commun.* 12 (2021) 3021, <https://doi.org/10.1038/s41467-021-23306-6>.
- L. Liu, X. Wu, L. Wang, X. Xu, L. Gan, Z. Si, J. Li, Q. Zhang, Y. Liu, Y. Zhao, R. Ran, X. Wu, D. Weng, F. Kang, Atomic palladium on graphitic carbon nitride as a hydrogen evolution catalyst under visible light irradiation, *Commun. Chem.* 2 (2019) 18, <https://doi.org/10.1038/s42004-019-0117-4>.
- H.-T. Vuong, T. Mahvelati-Shamsabadi, T.T. Dang, Q.D. Dao, E.W. Shin, J. S. Chung, Bandgap control of p-n heterojunction of Cu-Cu₂O @ ZnO with modified reduced graphene oxide nanocomposites for photocatalytic hydrogen evolution, *Int. J. Hydrog. Energ.* 47 (2022) 23249–23263, <https://doi.org/10.1016/j.ijhydene.2022.05.139>.
- W.-H. Fang, L. Zhang, J. Zhang, Synthetic strategies, diverse structures and tuneable properties of polyoxo-titanium clusters, *Chem. Soc. Rev.* 47 (2018) 404–421, <https://doi.org/10.1039/C7CS00511C>.
- J. Ran, J. Zhang, J. Yu, M. Jaroniec, S.Z. Qiao, Earth-abundant cocatalysts for semiconductor-based photocatalytic water splitting, *Chem. Soc. Rev.* 43 (2014) 7787–7812, <https://doi.org/10.1039/C3CS60425J>.
- J. Yang, D. Wang, H. Han, C. Li, Roles of cocatalysts in photocatalysis and photoelectrocatalysis, *Acc. Chem. Res.* 46 (2013) 1900–1909, <https://doi.org/10.1021/ar300227e>.
- D. Gao, H. Long, X. Wang, J. Yu, H. Yu, Tailoring antibonding-orbital occupancy state of selenium in Se-enriched ReSe_{2+x} cocatalyst for exceptional H₂ evolution of TiO₂ photocatalyst, *Adv. Funct. Mater.* 33 (2023) 2209994, <https://doi.org/10.1002/adfm.202209994>.
- Y. Wu, Z. Jiang, X. Lu, Y. Liang, H. Wang, Domino electroreduction of CO₂ to methanol on a molecular catalyst, *Nature* 575 (2019) 639–642, <https://doi.org/10.1038/s41586-019-1760-8>.
- X. Li, W. Bi, L. Zhang, S. Tao, W. Chu, Q. Zhang, Y. Luo, C. Wu, Y. Xie, Single-atom Pt as Co-catalyst for enhanced photocatalytic H₂ evolution, *Adv. Mater.* 28 (2016) 2427–2431, <https://doi.org/10.1002/adma.201505281>.
- D. Gao, J. Xu, F. Chen, P. Wang, H. Yu, Unsaturated selenium-enriched MoSe_{2+x} amorphous nanoclusters: one-step photoinduced co-reduction route and its boosted photocatalytic H₂-evolution activity for TiO₂, *Appl. Catal. B: Environ.* 305 (2022), 121053, <https://doi.org/10.1016/j.apcatb.2021.121053>.
- C. Zhang, H. Wang, H. Yu, K. Yi, W. Zhang, X. Yuan, J. Huang, Y. Deng, G. Zeng, Single-atom catalysts for hydrogen generation: rational design, recent advances, and perspectives, *Adv. Energy Mater.* 12 (2022) 2200875, <https://doi.org/10.1002/aenm.202200875>.
- D. Liu, A. Barbar, T. Najam, M.S. Javed, J. Shen, P. Tsiakaras, X. Cai, Single noble metal atoms doped 2D materials for catalysis, *Appl. Catal. B: Environ.* 297 (2021), 120389, <https://doi.org/10.1016/j.apcatb.2021.120389>.
- T. Lim, G.Y. Jung, J.H. Kim, S.O. Park, J. Park, Y.-T. Kim, S.J. Kang, H.Y. Jeong, S. K. Kwak, S.H. Joo, Atomically dispersed Pt-N₄ sites as efficient and selective electrocatalysts for the chlorine evolution reaction, *Nat. Commun.* 11 (2020) 412, <https://doi.org/10.1038/s41467-019-14272-1>.
- T. Lim, J.H. Kim, J. Kim, D.S. Baek, T.J. Shin, H.Y. Jeong, K.-S. Lee, K.S. Exner, S. H. Joo, General efficacy of atomically dispersed Pt catalysts for the chlorine evolution reaction: potential-dependent switching of the kinetics and mechanism, *ACS Catal.* 11 (2021) 12232–12246, <https://doi.org/10.1021/acscatal.1c03893>.
- J. Zhang, Y. Gu, Y. Lu, C. Zhu, G. Liu, C. Wang, D. Sun, Y. Tang, H. Sun, Each performs its own functions: nickel oxide supported ruthenium single-atoms and nanoclusters relay catalysis with multi-active sites for efficient alkaline hydrogen evolution reaction, *Appl. Catal. B: Environ.* 325 (2023), 122316, <https://doi.org/10.1016/j.apcatb.2022.122316>.
- X. Li, S. Zhao, X. Duan, H. Zhang, S.-z Yang, P. Zhang, S.P. Jiang, S. Liu, H. Sun, S. Wang, Coupling hydrothermal and photochemical single-atom catalysis toward excellent water splitting to hydrogen, *Appl. Catal. B: Environ.* 283 (2021), 119660, <https://doi.org/10.1016/j.apcatb.2020.119660>.
- B.-B. Xu, X.-B. Fu, X.-M. You, E. Zhao, F.-F. Li, Z. Chen, Y.-X. Li, X.L. Wang, Y.-F. Yao, Synergistic promotion of single-atom Co surrounding a PtCo alloy based on a g-C₃N₄ nanosheet for overall water splitting, *ACS Catal.* 12 (2022) 6958–6967, <https://doi.org/10.1021/acscatal.2c00751>.
- X. Li, Z. Hu, Q. Li, M. Lei, J. Fan, S.A.C. Carabineiro, Y. Liu, K. Lv, Three in one: atomically dispersed Na boosting the photoreactivity of carbon nitride towards NO oxidation, *Chem. Commun.* 56 (2020) 14195–14198, <https://doi.org/10.1039/D0CC05948J>.
- M.B. Boucher, B. Zugic, G. Cladaras, J. Kammert, M.D. Marcinkowski, T.J. Lawton, E.C.H. Sykes, M. Flytzani-Stephanopoulos, Single atom alloy surface analogs in Pd_{0.18}Cu_{1.5} nanoparticles for selective hydrogenation reactions, *Phys. Chem. Chem. Phys.* 15 (2013) 12187–12196, <https://doi.org/10.1039/C3CP51538A>.
- J. Gu, M. Jian, L. Huang, Z. Sun, A. Li, Y. Pan, J. Yang, W. Wen, W. Zhou, Y. Lin, H.-J. Wang, X. Liu, L. Wang, X. Shi, X. Huang, L. Cao, S. Chen, X. Zheng, H. Pan, J. Zhu, S. Wei, W.-X. Li, J. Lu, Synergizing metal-support interactions and spatial confinement boosts dynamics of atomic nickel for hydrogenations, *Nat. Nanotechnol.* 16 (2021) 1141–1149, <https://doi.org/10.1038/s41565-021-00951-y>.
- J.H. Kwak, J. Hu, D. Mei, C.-W. Yi, D.H. Kim, C.H.F. Peden, L.F. Allard, J. Szanyi, Coordinatively Unsaturated Al³⁺ Centers as Binding Sites for Active Catalyst Phases of Platinum on γ-Al₂O₃, *Science* 325 (2009) 1670–1673, <https://doi.org/10.1126/science.1176745>.

- [26] B.-H. Lee, E. Gong, M. Kim, S. Park, H.R. Kim, J. Lee, E. Jung, C.W. Lee, J. Bok, Y. Jung, Y.S. Kim, K.-S. Lee, S.-P. Cho, J.-W. Jung, C.-H. Cho, S. Lebegue, K.T. Nam, H. Kim, S.-I. In, T. Hyeon, Electronic interaction between transition metal single-atoms and anatase TiO₂ boosts CO₂ photoreduction with H₂O, *Energy Environ. Sci.* 15 (2022) 601–609, <https://doi.org/10.1039/D1EE01574E>.
- [27] Y. Chen, Z. Huang, P. Hu, J. Chen, X. Tang, Improved performance of supported single-atom catalysts via increased surface active sites, *Catal. Commun.* 75 (2016) 74–77, <https://doi.org/10.1016/j.catcom.2015.11.021>.
- [28] J. Li, Q. Guan, H. Wu, W. Liu, Y. Lin, Z. Sun, X. Ye, X. Zheng, H. Pan, J. Zhu, S. Chen, W. Zhang, S. Wei, J. Lu, Highly active and stable metal single-atom catalysts achieved by strong electronic metal–support interactions, *J. Am. Chem. Soc.* 141 (2019) 14515–14519, <https://doi.org/10.1021/jacs.9b06482>.
- [29] B.D. Chandler, Strong metal-support interactions: an extra layer of complexity, *Nat. Chem.* 9 (2017) 108, <https://doi.org/10.1038/nchem.2724>.
- [30] X. Hai, X. Zhao, N. Guo, C. Yao, C. Chen, W. Liu, Y. Du, H. Yan, J. Li, Z. Chen, X. Li, Z. Li, H. Xu, P. Lyu, J. Zhang, M. Lin, C. Su, S.J. Pennycook, C. Zhang, S. Xi, J. Lu, Engineering local and global structures of single co atoms for a superior oxygen reduction reaction, *ACS Catal.* 10 (2020) 5862–5870, <https://doi.org/10.1021/acscatal.0c00936>.
- [31] K. Naveen, T. Mahvelati-Shamsabadi, P. Sharma, S.-h Lee, S.H. Hur, W.M. Choi, T. J. Shin, J.S. Chung, MOF-derived Co/Zn single-atom catalysts for reversible hydrogenation and dehydrogenation of quinoline hydrogen carrier, *Appl. Catal. B: Environ.* 328 (2023), 122482, <https://doi.org/10.1016/j.apcatb.2023.122482>.
- [32] C. Zhu, Y. Nie, F. Cun, Y. Wang, Z. Tian, F. Liu, Two-step pyrolysis to anchor ultrahigh-density single-atom FeN₅ sites on carbon nitride for efficient Fenton-like catalysis near 0 °C, *Appl. Catal. B: Environ.* 319 (2022), 121900, <https://doi.org/10.1016/j.apcatb.2022.121900>.
- [33] R. Qin, P. Liu, G. Fu, N. Zheng, Strategies for stabilizing atomically dispersed metal catalysts, *Small Methods* 2 (2018) 1700286, <https://doi.org/10.1002/smtd.201700286>.
- [34] R. Li, D. Wang, Superiority of dual-atom catalysts in electrocatalysis: one step further than single-atom catalysts, *Adv. Energy Mater.* 12 (2022) 2103564, <https://doi.org/10.1002/aenm.202103564>.
- [35] M.A.R. da Silva, I.F. Silva, Q. Xue, B.T.W. Lo, N.V. Tarakina, B.N. Nunes, P. Adler, S.K. Sahoo, D.W. Bahnemann, N. López-Salas, A. Savateev, C. Ribeiro, T.D. Kühne, M. Antonietti, I.F. Teixeira, Sustainable oxidation catalysis supported by light: Fe-poly (heptazine imide) as a heterogeneous single-atom photocatalyst, *Appl. Catal. B: Environ.* 304 (2022), 120965, <https://doi.org/10.1016/j.apcatb.2021.120965>.
- [36] Z. Li, M. Zhang, X. Dong, S. Ji, L. Zhang, L. Leng, H. Li, J.H. Horton, Q. Xu, J. Zhu, Strong electronic interaction of indium oxide with palladium single atoms induced by quenching toward enhanced hydrogenation of nitrobenzene, *Appl. Catal. B: Environ.* 313 (2022), 121462, <https://doi.org/10.1016/j.apcatb.2022.121462>.
- [37] J. Hulva, M. Meier, R. Bliem, Z. Jakub, F. Kraushofer, M. Schmid, U. Diebold, C. Franchini, G.S. Parkinson, Unraveling CO adsorption on model single-atom catalysts, *Science* 371 (2021) 375–379, <https://doi.org/10.1126/science.abe5757>.
- [38] L. DeRita, J. Resasco, S. Dai, A. Boubnov, H.V. Thang, A.S. Hoffman, I. Ro, G. W. Graham, S.R. Bare, G. Pacchioni, X. Pan, P. Christopher, Structural evolution of atomically dispersed Pt catalysts dictates reactivity, *Nat. Mater.* 18 (2019) 746–751, <https://doi.org/10.1038/s41563-019-0349-9>.
- [39] Z. Teng, Q. Zhang, H. Yang, K. Kato, W. Yang, Y.-R. Lu, S. Liu, C. Wang, A. Yamakata, C. Su, B. Liu, T. Ohno, Atomically dispersed antimony on carbon nitride for the artificial photosynthesis of hydrogen peroxide, *Nat. Catal.* 4 (2021) 374–384, <https://doi.org/10.1038/s41929-021-00605-1>.
- [40] T.T. Dang, T.K.A. Nguyen, K.C. Bhamu, T. Mahvelati-Shamsabadi, V.K.H. Van, E. W. Shin, K.-H. Chung, S.H. Hur, W.M. Choi, S.G. Kang, J.S. Chung, Engineering hole defects on 2D graphitic carbon nitride nanosheets by solvolysis in organic solvents, *ACS Catal.* 12 (2022) 13763–13780, <https://doi.org/10.1021/acscatal.2c03523>.
- [41] H. Fattahimoghaddam, T. Mahvelati-Shamsabadi, C.-S. Jeong, B.-K. Lee, Coral-like potassium and phosphorous doped graphitic carbon nitride structures with enhanced charge and mass transfer dynamics toward photocatalytic hydrogen peroxide production and microbial disinfection, *J. Colloid Interface Sci.* 617 (2022) 326–340, <https://doi.org/10.1016/j.jcis.2022.03.027>.
- [42] T. Mahvelati-Shamsabadi, B.-K. Lee, Photocatalytic H₂ evolution and CO₂ reduction over phosphorus-doped g-C₃N₄ nanostructures: Electronic, Optical, and Surface properties, *Renew. Sustain. Energy Rev.* 130 (2020), 109957, <https://doi.org/10.1016/j.rser.2020.109957>.
- [43] T. Mahvelati-Shamsabadi, H. Fattahimoghaddam, B.-K. Lee, H. Ryu, J.I. Jang, Caesium sites coordinated in Boron-doped porous and wrinkled graphitic carbon nitride nanosheets for efficient charge carrier separation and Transfer: Photocatalytic H₂ and H₂O₂ production, *Chem. Eng. J.* 423 (2021), 130067, <https://doi.org/10.1016/j.cej.2021.130067>.
- [44] K. Li, W. Zhou, X. Li, Q. Li, S.A.C. Carabineiro, S. Zhang, J. Fan, K. Lv, Synergistic effect of cyano defects and CaCO₃ in graphitic carbon nitride nanosheets for efficient visible-light-driven photocatalytic NO removal, *J. Hazard. Mater.* 442 (2023), 130040, <https://doi.org/10.1016/j.jhazmat.2022.130040>.
- [45] J. Chen, K. Li, X. Li, J.-J. Fan, K. Lv, Preparation and modification of crystalline carbon nitride, *Chin. J. Inorg. Chem.* 37 (2021) 1713–1726, <https://doi.org/10.11862/CJIC.2021.206>.
- [46] T. Mahvelati-Shamsabadi, H. Fattahimoghaddam, B.-K. Lee, S. Bae, J. Ryu, Synthesis of hexagonal rosettes of g-C₃N₄ with boosted charge transfer for the enhanced visible-light photocatalytic hydrogen evolution and hydrogen peroxide production, *J. Colloid Interface Sci.* 597 (2021) 345–360, <https://doi.org/10.1016/j.jcis.2021.04.019>.
- [47] H. Fattahimoghaddam, T. Mahvelati-Shamsabadi, B.-K. Lee, Enhancement in photocatalytic H₂O₂ production over g-C₃N₄ nanostructures: a collaborative approach of nitrogen deficiency and supramolecular precursors, *ACS Sustain. Chem. Eng.* 9 (2021) 4520–4530, <https://doi.org/10.1021/acssuschemeng.0c08884>.
- [48] H. Fattahimoghaddam, T. Mahvelati-Shamsabadi, B.-K. Lee, Efficient photodegradation of rhodamine B and tetracycline over robust and green g-C₃N₄ nanostructures: supramolecular design, *J. Hazard. Mater.* 403 (2021), 123703, <https://doi.org/10.1016/j.jhazmat.2020.123703>.
- [49] M. Razavi-Esfali, T. Mahvelati-Shamsabadi, H. Fattahimoghaddam, B.-K. Lee, Highly efficient photocatalytic degradation of organic pollutants by mesoporous graphitic carbon nitride bonded with cyano groups, *Chem. Eng. J.* 419 (2021), 129503, <https://doi.org/10.1016/j.cej.2021.129503>.
- [50] H. Ou, X. Chen, L. Lin, Y. Fang, X. Wang, Biomimetic donor–acceptor motifs in conjugated polymers for promoting exciton splitting and charge Separation, *Angew. Chem. Int. Ed.* 57 (2018) 8729–8733, <https://doi.org/10.1002/anie.201803863>.
- [51] J.H. Kim, D. Shin, J. Lee, D.S. Baek, T.J. Shin, Y.-T. Kim, H.Y. Jeong, J.H. Kwak, H. Kim, S.H. Joo, A general strategy to atomically dispersed precious metal catalysts for unravelling their catalytic trends for oxygen reduction reaction, *ACS Nano* 14 (2020) 1990–2001, <https://doi.org/10.1021/acsnano.9b08494>.
- [52] S. Tauster, S. Fung, R. Baker, J. Horsley, Strong interactions in supported-metal catalysts, *Science* 211 (1981) 1121–1125, <https://doi.org/10.1126/science.211.4487.1121>.
- [53] M. Vaarkamp, J.T. Miller, F.S. Modica, D.C. Koningsberger, On the relation between particle morphology, structure of the metal-support interface, and catalytic properties of Pt/γ-Al₂O₃, *J. Catal.* 163 (1996) 294–305, <https://doi.org/10.1006/jcat.1996.0330>.
- [54] P. Wang, X. Zhang, J. Zhang, S. Wan, S. Guo, G. Lu, J. Yao, X. Huang, Precise tuning in platinum-nickel/nickel sulfide interface nanowires for synergistic hydrogen evolution catalysis, *Nat. Commun.* 8 (2017) 14580, <https://doi.org/10.1038/ncomms14580>.
- [55] J.K. Nørskov, T. Bligaard, A. Logadottir, J. Kitchin, J.G. Chen, S. Pandalov, U. Stimming, Trends in the exchange current for hydrogen evolution, *J. Electrochem. Soc.* 152 (2005) J23, <https://doi.org/10.1149/1.1856988>.
- [56] G. Henkelman, B.P. Uberuaga, H. Jónsson, A climbing image nudged elastic band method for finding saddle points and minimum energy paths, *J. Chem. Phys.* 113 (2000) 9901–9904, <https://doi.org/10.1063/1.1329672>.